Article

Not peer-reviewed version

Coupled Aerostructural Optimization of a Composite Low Reynolds Wing Using Surrogate Modeling Techniques

Eleftherios Nikolaou [*], Spyridon Kilimtzidis [*], Panagiota Kelverkloglou [†], Vaios Lappas [†], Vassilis Kostopoulos [†]

Posted Date: 25 March 2026

doi: 10.20944/preprints202603.1960.v1

Keywords: aerostructural optimization; surrogate-based optimization (SBO); low-reynolds-number aerodynamics; UAV wing design; composite structures; CFD–FEM coupling; preliminary aircraft design; multi-disciplinary design optimization (MDO); wing planform optimization; structural weight minimization

 doi:10.20944/preprints202603.1960.v1

Article

Coupled Aerostructural Optimization of a Composite Low Reynolds Wing Using Surrogate Modeling Techniques

Eleftherios Nikolaou [1,*], Spyridon Kilimtzidis [1,*], Panagiota Kelverkloglou [1,†], Vaios Lappas [2,†] and Vassilis Kostopoulos [1,†]

[1] Applied Mechanics Laboratory, Mechanical Engineering and Aeronautics Department, University of Patras, Rio Campus, 26500 Patras, Greece
[2] Department of Aerospace Science and Technology, National and Kapodistrian University of Athens, 10679 Athens, Greece
* Correspondence: eleftherios_nikolaou@ac.upatras.gr (E.N.); s.kilimtzidis@ac.upatras.gr (S.K.)
† These authors contributed equally to this work.

Abstract

This study presents a coupled aerostructural optimization framework for the preliminary design of a low-Reynolds-number composite UAV wing, aiming to simultaneously enhance aerodynamic efficiency and structural performance. While previous work has primarily addressed aerodynamic optimization in isolation, the present approach integrates high-fidelity Computational Fluid Dynamics (CFD) and Finite Element Method (FEM) analyses within a Surrogate-Based Optimization (SBO) framework. The design space includes both aerodynamic parameters—aspect ratio, taper ratio, sweep angle, and twist—and structural variables related to the internal wing layout and component thicknesses. To reduce the computational cost associated with high-fidelity simulations, Kriging surrogate models are employed in conjunction with an Expected Improvement (EI) infill strategy, enabling efficient exploration of the coupled design space. The framework is evaluated through multiple independent optimization runs using different initial sampling strategies, demonstrating consistent convergence toward feasible high-performance designs. The surrogate models exhibit strong predictive capability, as confirmed by Root Mean Square Error (RMSE) and Leave-One-Out (LOO) cross-validation metrics. The results indicate that aerodynamic variables, particularly aspect ratio and twist, are the primary drivers of range performance. However, structural variables—most notably skin thickness—strongly influence constraint satisfaction, especially with respect to buckling and strength requirements, and therefore play a key role in defining the feasible design space. The optimal configuration achieves a maximum range of approximately 203 km while satisfying all strength, stiffness, and aerodynamic constraints. Overall, the proposed methodology provides an efficient and robust tool for early-stage aerostructural design of low-Reynolds-number UAV wings.

Keywords: aerostructural optimization; surrogate-based optimization (SBO); low-reynolds-number aerodynamics; UAV wing design; composite structures; CFD–FEM coupling; preliminary aircraft design; multi-disciplinary design optimization (MDO); wing planform optimization; structural weight minimization

1. Introduction

The wing plays a fundamental role in determining the overall performance of an aircraft, as aerodynamic efficiency and structural weight are strongly coupled through the wing geometry and internal layout. Key performance metrics, such as the lift-to-drag ratio (L/D) and take-off weight, are directly influenced by aerodynamic characteristics and structural efficiency. Consequently, careful wing design and optimization are essential to achieving an effective and well-balanced aircraft configuration. During the preliminary design phase, the aerodynamic efficiency of the wing largely dictates the

 doi:10.20944/preprints202603.1960.v1

expected performance of the complete aircraft, making early-stage wing optimization a critical step in guiding subsequent design decisions.

Aircraft designers therefore aim to identify optimal configurations from both aerodynamic and structural perspectives. Aerodynamic performance is influenced by parameters such as aspect ratio (AR), taper ratio (λ), sweep angle (Λ), and twist (ϵ), while the structural configuration is governed by material selection, internal layout (e.g., ribs and spars), and the thickness of structural components, all of which significantly affect the final weight and structural performance.

Over the past decades, numerous studies have investigated various aspects of wing optimization. From an aerodynamic perspective, Lyu et al. [1] performed aerodynamic shape optimization of a benchmark wing using a gradient-based algorithm coupled with Reynolds-Averaged Navier–Stokes (RANS) equations and the Spalart–Allmaras turbulence model. Similarly, Chen et al. [2] optimized the aerodynamic shape of the Common Research Model (CRM) wing-body-tail configuration under trim constraints. Additional contributions include the work of Ghafoorian et al. [3], who optimized wind turbine blades, and Zheng et al. [4], who applied manifold learning techniques to aerodynamic shape design optimization.

On the structural side, optimization has traditionally focused on minimizing mass while satisfying strength, stiffness, and stability constraints. The introduction of composite materials has significantly expanded the design space by incorporating additional variables such as ply orientation, thickness, and stacking sequence, motivating the development of advanced optimization methodologies [5,6]. Early studies employed direct ply-based optimization approaches, while later work introduced lamination parameters to enable continuous design spaces and improve numerical efficiency [7–9]. More recent research has emphasized the importance of geometric nonlinearities in high-aspect-ratio wing structures, demonstrating that linear models tend to overestimate loads and lead to conservative designs [10,11]. Incorporating nonlinear structural behavior has been shown to yield lighter configurations without compromising aerodynamic performance.

Combined, these approaches form aerostructural optimization, which seeks to simultaneously improve aerodynamic and structural performance by accounting for the strong coupling between aerodynamic loads and structural deformation, particularly in flexible wing configurations. Early aerostructural optimization frameworks relied on low-fidelity aerodynamic models, such as lifting-line theory, panel methods, and the doublet lattice method, coupled with simplified structural representations, enabling efficient design space exploration at low computational cost [12–17]. With increasing computational capabilities, high-fidelity approaches have emerged, combining Euler or RANS-based CFD solvers with detailed Finite Element Method (FEM) structural models, allowing accurate prediction of aeroelastic effects and load redistribution [18–22]. However, the high computational cost of such approaches limits their applicability during early design stages. Consequently, recent research has focused on multi-fidelity and surrogate-based strategies, which balance computational efficiency and accuracy by combining low- and high-fidelity models [23–25].

Surrogate-based optimization (SBO) methods have been widely applied to aerostructural problems. Nikolaou et al. [26] applied SBO techniques to optimize UAV winglet geometry, while Benaouali and Kachel [27] developed a Multidisciplinary Design Optimization (MDO) framework integrating commercial tools, initially focusing on airfoil optimization and subsequently on overall wing performance.

Despite this extensive body of work, the low-Reynolds-number regime remains comparatively underexplored, as most studies focus on conventional subsonic configurations. Furthermore, high-fidelity aerostructural optimization frameworks are computationally expensive and are therefore rarely applied in early-stage design for UAV applications.

To overcome these limitations, the present study proposes a coupled aerostructural optimization framework tailored to low-Reynolds-number UAV wings. Building upon previous work in which a multi-fidelity optimization framework was used to identify an aerodynamically optimal configuration [28], the current study extends this approach by incorporating both aerodynamic and structural

 doi:10.20944/preprints202603.1960.v1

considerations, ensuring consistency and comparability of results. The main contributions of this study can be summarized as follows:

- Development of a high-fidelity aerostructural optimization framework integrating CFD and FEM analyses within a surrogate-based optimization (SBO) approach.
- Simultaneous optimization of aerodynamic and structural design variables, including planform parameters and internal wing layout characteristics.
- Application of Kriging surrogate models with an Expected Improvement (EI) strategy to efficiently explore the coupled design space.
- Systematic assessment of surrogate accuracy and optimization robustness through multiple independent runs and validation metrics.
- Identification of the dominant design drivers governing range performance and constraint satisfaction in low-Reynolds-number UAV wings.

The proposed optimization framework employs a high-fidelity surrogate-based optimization (SBO) approach, coupled with Computational Fluid Dynamics (CFD) and Finite Element Method (FEM) analyses. The objective is to maximize aircraft range, subject to constraints on the cruise lift coefficient ($C_{L_{cruise}}$), structural strength via the maximum Failure Index (FI_{max}), and stiffness via the first global buckling eigenvalue (λ_1). The design space includes twelve variables, comprising four aerodynamic parameters—aspect ratio, taper ratio, sweep angle, and tip twist—and eight structural parameters related to internal layout and component thicknesses. Surrogate model accuracy is evaluated using Root Mean Square Error (RMSE) and Leave-One-Out cross-validation metrics, while robustness is assessed through five different Design of Experiments (DoE) strategies.

The remainder of this paper is organized as follows. Section 2 presents the methodological framework, including the CFD and FEM models, the surrogate modeling approach, and the optimization setup. Section 3 reports and analyzes the results of the aerostructural optimization, including surrogate model accuracy and optimal configurations. Section 4 discusses the key findings and concludes the study.

2. Materials and Methods

2.1. Baseline Aircraft Specifications and Requirements

The design process begins with the definition of the mission flight characteristics and the operational requirements of the aircraft. Within the framework of this study, an Unmanned Aerial Vehicle (UAV) has been selected as the case study. According to the NATO classification system for UAVs, the aircraft in this study falls into the Class I mini UAV category. Table 1 presents the key UAV parameters that serve as the basis for the aerodynamic optimization and design framework. The developed UAV is presented in Figure 1.

Table 1. UAV requirements and mission flight characteristics.

Characteristic	Symbol
UAV type	Fixed-wing
Propulsion system	Battery-powered electric
Wingspan	$\leq 3\ m$
UAV length	$\leq 1.5\ m$
Maximum take-off weight	$\leq 15\ kg$
Take-off	Catapult take-off
Cruise speed	$\geq 22\ m/s$
Loiter Speed	$\geq 20\ m/s$
Climb Speed	$\geq 1.2 \times V_{stall}$
Operational altitude	$1500m\ ASL$

 doi:10.20944/preprints202603.1960.v1

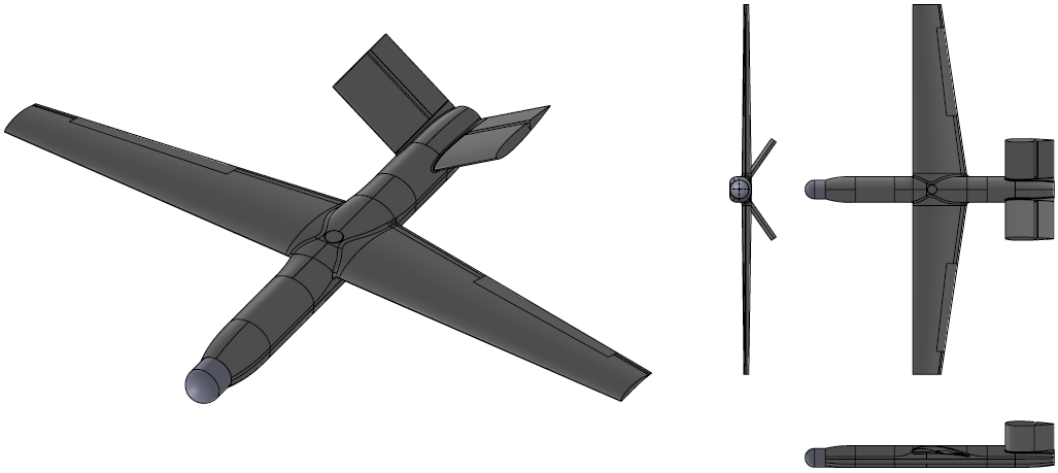

Figure 1. Baseline UAV configuration.

2.2. High-Fidelity CFD Aerodynamics

A numerical model of a wing, incorporating the average values of key geometric characteristics, was developed as the foundation for subsequent Computational Fluid Dynamics (CFD) analyses and optimization studies of various wing configurations derived from the surrogate model. The computational domain dimensions and boundary conditions were carefully designed to reflect the UAV's operational environment and altitude. Simulations were conducted using ANSYS Fluent [29], solving the Reynolds-Averaged Navier-Stokes (RANS) equations coupled with the Spalart-Allmaras turbulence model [30]. The Spalart–Allmaras model was selected due to its robustness and proven performance in predicting attached and mildly separated flows at low Reynolds numbers, making it suitable for UAV aerodynamic analysis. The computational domain was defined as a rectangular region measuring $6.0 \times 4.0 \times 10.0$ m. The RANS equations were discretized using the Finite Volume Method (FVM) under incompressible, steady-state flow assumptions with an appropriately refined mesh. To ensure accurate boundary layer resolution, a first cell wall distance of $Y^+ \approx 1$ was achieved, with the initial layer height set to $y = 7.4 \times 10^{-5}$ m. A mesh independence study was also conducted to verify that further refinement did not impact the results, ensuring an optimal balance between accuracy and computational efficiency. The computational domain, including dimensions, boundary conditions, and mesh details, is illustrated in Figures 2 and 3.

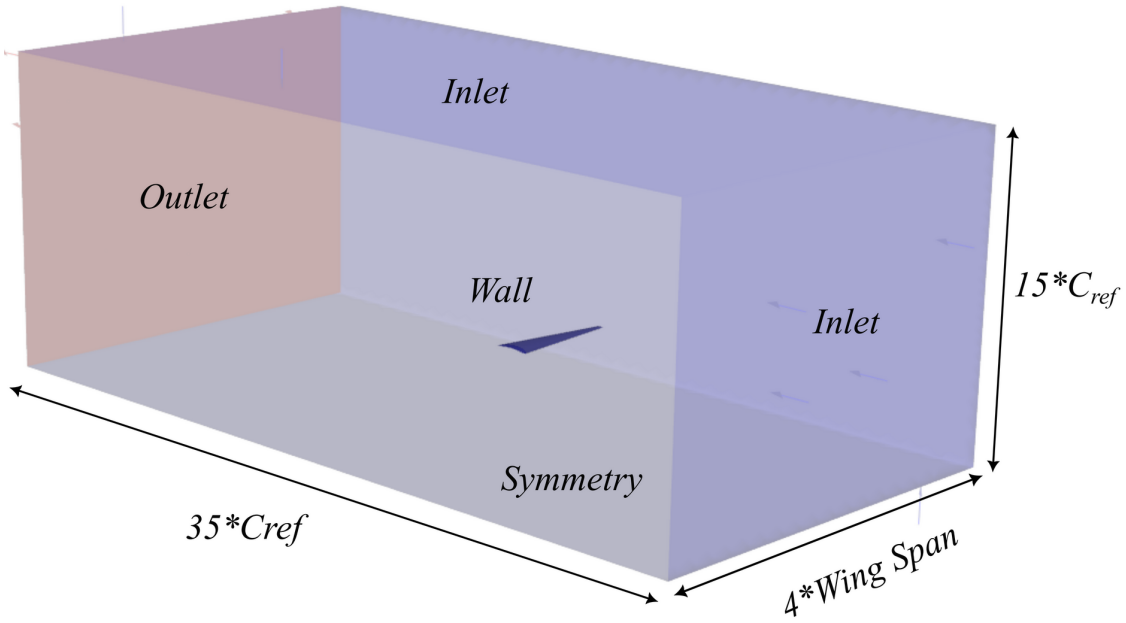

Figure 2. CFD domain characteristics.

 doi:10.20944/preprints202603.1960.v1

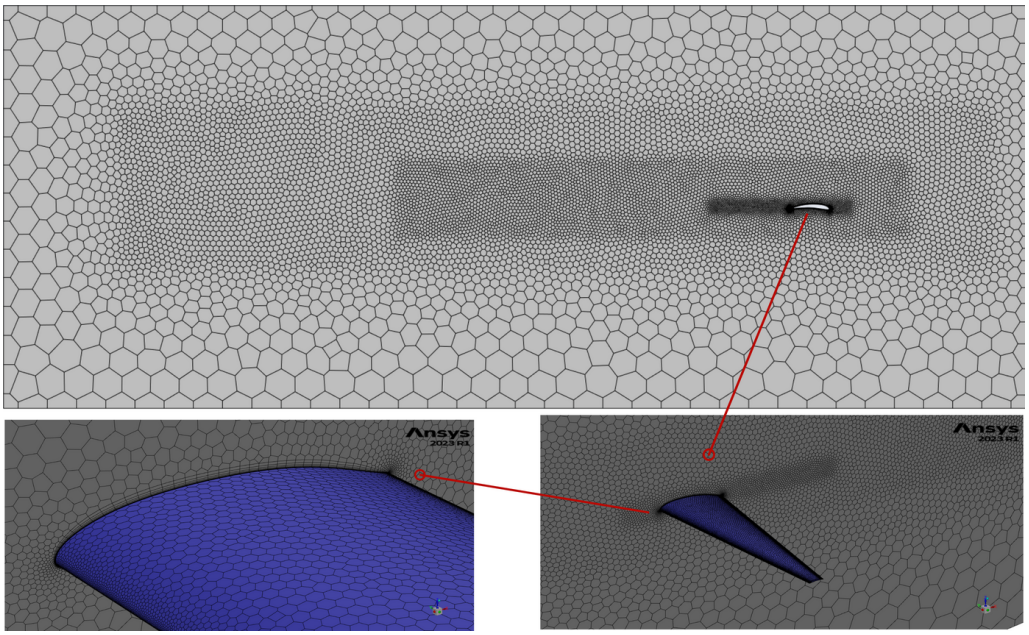

Figure 3. CFD mesh around the wing.

Pressure and temperature values were set according to the UAV's maximum operating altitude, with a predefined inlet velocity. The outlet boundary conditions were defined with a zero pressure gradient, while the turbulence intensity was set to 1%. A symmetry boundary condition was applied along the longitudinal plane, and the wing surfaces were modeled as free-slip walls. The convergence of the lift and drag coefficients, C_L and C_D, respectively, is illustrated in Figure 4, while Figure 5 illustrates the Y^+ distribution for each model of the mesh independence study.

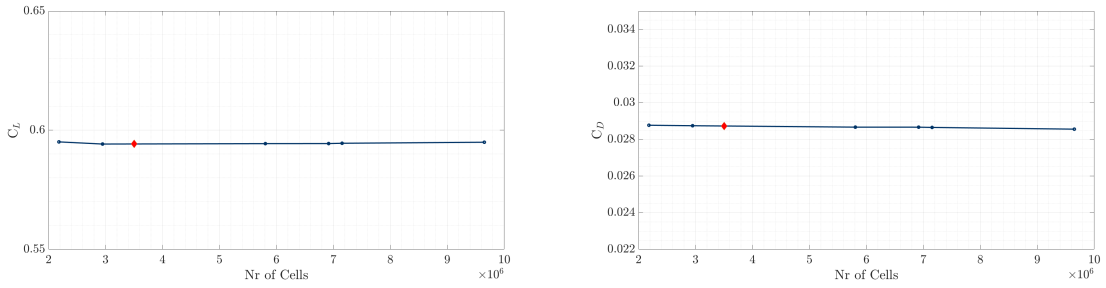

(a) **(b)**

Figure 4. C_L and C_D vs number of domain cells – Mesh independence study.

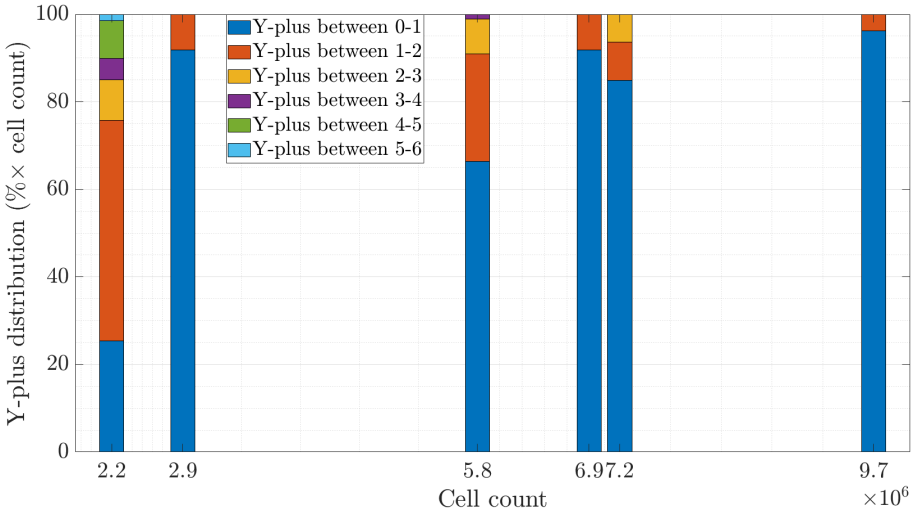

Figure 5. Y^+ distribution - Mesh independence study.

 doi:10.20944/preprints202603.1960.v1

2.3. FEM Model

The FE model of the wing is generated based on the external surfaces of the UAV. The model is generated in NASTRAN, and for the skins, spars, and ribs, 4-noded quadrilateral shell elements (CQUAD4) are used, while for the spar caps and stringers beam elements (CBEAM), accounting also for the relevant offset values. As a datum design point, a cross-ply, two-layered laminate, consisting of a 0^0 and a 90^0 ply, has been considered for all the relevant wing parts. The Hexcel IM7/8552 composite material system is selected for the relevant parts of the wing, with the respective B-Basis material properties, strength values and cured ply thickness listed in Table 2. For the beam elements and to simplify the analysis, rectangular cross-sections are considered. The respective thickness, nevertheless, is calculated based on the aforementioned laminate, since they are also considered to be manufactured of the provided composite material. However, only isotropic materials are allowed for the definition of the CBEAM elements. As a result, and since the baseline lay-up is symmetric, equivalent laminate axial and shear moduli, E_{eq} and G_{eq} respectively, can be calculated based on the following Equations 1 and 2 [31]:

$$E_{eq} = \frac{1}{t}(A_{11} - \frac{A_{12}^2}{A_{22}}) \tag{1}$$

$$G_{eq} = \frac{A_{66}}{t} \tag{2}$$

where t the thickness, A_{11}, A_{12}, A_2 and A_{66} the corresponding terms of the extensional stiffness matrix of a laminate. Regarding the boundary conditions, the wing is assumed to be clamped at its root section, thus fixing all relative nodal Degrees of Freedom (D.o.F). The resulting FEM mesh of the wing model is presented in Figure 6.

Table 2. Composite Materials Properties [32].

Material System	**Hexcel IM7/8552**
E_1, GPa	158.51
E_2, GPa	8.96
G_{12}, GPa	4.68
ν_{12}, GPa	0.31
X_T, MPa	2500
X_C, MPa	1531
Y_T, MPa	640.5
Y_C, MPa	285.7
S, MPa	53.5
Ply thickness, m	1.8288×10^{-4}

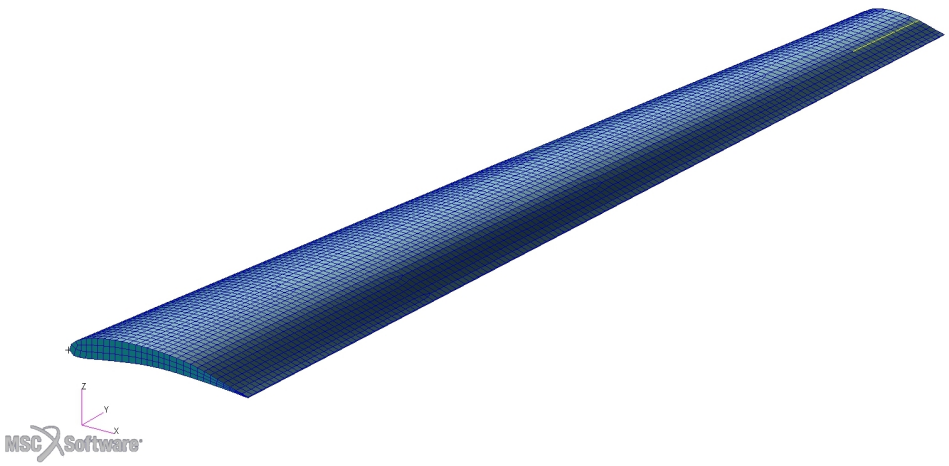

Figure 6. FEM mesh of the wing

 doi:10.20944/preprints202603.1960.v1

2.4. Surrogate Modeling

The key steps in a typical SBO process, as outlined in Alexandrov et al. [33], include:

- Sampling the design space and evaluating the objective function along with any constraints.
- Constructing the surrogate model based on the sampled data.
- Searching the design space and refining the surrogate model using update (infill) criteria.
- Enhancing the model by incorporating newly added points and repeating the process.

The sampling stage is a crucial step in an SBO algorithm, as the surrogate model's accuracy depends on the selection of initial design points. To ensure the model represents the design space effectively, the most influential points must be chosen to maximize the information available for surrogate construction. Given the often high-dimensional nature of design problems, exhaustive grid searches become computationally prohibitive. Instead, more efficient techniques, such as Latin Hypercube Sampling (LHS) [34], are commonly used. LHS is a robust statistical method that generates parameter samples from a multidimensional distribution while maintaining a well-distributed design space representation. The method involves an optimization problem aimed at maximizing the distance between sample points while ensuring each coordinate follows a predefined probability distribution. Once the sampling is completed, the next step is to construct the surrogate model, typically represented as a general function:

$$\hat{f}(\mathbf{x}, w) \tag{3}$$

where w denotes model parameters, and $\mathbf{x}$ represents the design variables. A key criterion for selecting a surrogate model is its ability to accurately capture the desired function's characteristics while maintaining flexibility. Overly rigid models risk instability and overfitting. One widely used surrogate model in engineering applications is Kriging [35,36], which expresses function approximations as a linear combination of basis functions (kernels) that depend on the Euclidean distance between design points. For noise-free data, the Kriging approximation is given by:

$$\hat{f}(\mathbf{x}) = \sum_{i=1}^{N} w_i \, \psi\left(\|\mathbf{x} - \mathbf{x}^{(i)}\| \right) \tag{4}$$

where:

- N_c is the number of basis functions,
- $\mathbf{x}_c^{(n)}$ represents the center of the n-th basis function,
- $\psi(||\mathbf{x} - \mathbf{x}_c^{(n)}||)$ is the kernel function, evaluated based on the distance between the prediction point $\mathbf{x}$ and the corresponding center.

The kernel function is typically defined as:

$$\psi\left(\|\mathbf{x} - \mathbf{x}^{(i)}\| \right) = \exp\left(- \sum_{k=1}^{d} \theta_k \left| x_k - x_k^{(i)} \right|^{p_k} \right) \tag{5}$$

where θ_n and p_n are model parameters.

The Kriging model is constructed using the following steps:

- Formulating the correlation matrix based on training data points:

$$[\Psi]_{ij} = \exp\left(- \sum_{k=1}^{d} \theta_k \left| x_k^{(i)} - x_k^{(j)} \right|^{p_k} \right) \tag{6}$$

- Maximizing the Maximum Likelihood Estimator (MLE):

$$\ln(MLE) = -\frac{n}{2} \ln(\hat{\sigma}^2) - \frac{1}{2} \ln([\Psi]) \tag{7}$$

 doi:10.20944/preprints202603.1960.v1

where $\hat{\sigma}$ is the MLE estimate of the standard deviation.

- Predicting values at new design points:

$$\hat{y}(\mathbf{x}) = \hat{\mu} + \mathbf{r}^T(\mathbf{x})\,\boldsymbol{\Psi}^{-1}(\mathbf{y} - \mathbf{1}\hat{\mu}) \tag{8}$$

where $\mathbf{r}(\mathbf{x})$ is the correlation vector between the prediction point and the sampled data points. For Gaussian-based processes, the Mean Squared Error (MSE) estimation is given by:

$$\hat{s}(\mathbf{x})^2 = \hat{\sigma}^2\left(1 - \boldsymbol{\psi}^T[\Psi]^{-1}\boldsymbol{\psi} + \frac{1 - \mathbf{1}^T[\Psi]^{-1}\boldsymbol{\psi}}{\mathbf{1}^T[\Psi]^{-1}\mathbf{1}}\right) \tag{9}$$

A commonly used approach for improvement is the Expected Improvement (EI) function:

$$E[I(\mathbf{x})] = (y_{\min} - \hat{y}(\mathbf{x}))\,\Phi\left(\frac{y_{\min} - \hat{y}(\mathbf{x})}{\hat{s}(\mathbf{x})}\right) + \hat{s}(\mathbf{x})\,\phi\left(\frac{y_{\min} - \hat{y}(\mathbf{x})}{\hat{s}(\mathbf{x})}\right) \tag{10}$$

where Φ and ϕ denote the cumulative distribution and probability density functions, respectively. As an additional step toward more realistic SBO frameworks, constraints should be incorporated into the surrogate model. The approach to constraint handling depends on the computational cost of evaluating the constraint function. Constraints can either be evaluated directly or modeled using surrogate techniques similar to those applied to the objective function, effectively creating a surrogate model for each constraint. When constraint evaluations are computationally inexpensive, conventional constraint optimization methods, in conjunction with the objective function surrogate model, guide the SBO framework toward both promising and feasible regions of the design space. However, if surrogate models are also employed for constraints, the expected improvement function from Equation (10) is modified into the constrained expected improvement function by introducing the probability of feasibility:

$$P[F(\mathbf{x})] = \Phi\left(\frac{0 - \hat{g}(\mathbf{x})}{\hat{s}_g(\mathbf{x})}\right) \tag{11}$$

where F represents the feasibility measure of a constraint g, and $\hat{s_g}$ denotes the variance of the constraint's Kriging model. The probability of achieving an improvement over the current minimum function value while satisfying feasibility conditions is then determined by multiplying Equations (10) and (11):

$$E[I(\mathbf{x}) \cap F(\mathbf{x})] = E[I(\mathbf{x})] \cdot P[F(\mathbf{x})] \tag{12}$$

To determine the next point for model refinement, a sub-optimization problem is solved:

$$\mathbf{x}_{\text{infill}} = \arg\max(E[I(\mathbf{x})] \cdot P[F(\mathbf{x})]) \tag{13}$$

This function depends on the Kriging model parameters, θ_n and p_n; while optimizing both the correlation length parameters, θ_n and the exponents p_n can improve prediction accuracy in many applications, and doing so increases the complexity of the optimization process. To simplify the model calibration and reduce computational costs, we follow the approach commonly adopted in the surrogate modeling literature [35–37] and fix the value of $p_n = 2$, corresponding to a Gaussian correlation function. This allows us to focus on tuning θ_n alone, using a global optimization method, which, in our case, is a genetic algorithm, as implemented in Python. The particular optimization was executed for 1000 iterations. As noted by Forrester et al. [37], searching for θ_n on a logarithmic scale, typically within the bounds 10^{-3} to 10^2, is effective. It is also recommended to scale the input design space to [0, 1] to ensure consistent interpretability of the parameter values across different problems.

The resulting point, $\mathbf{x}_{\text{infill}}$, is then added in the current dataset, which is then re-trained. This process is typically repeated for a predefined number of iterations. Within the present study, a samples-to-infill points ratio of 1:2 was selected as recommended in [36]. This ensures that the surrogate model is updated efficiently, balancing exploration and exploitation for improved optimization performance.

 doi:10.20944/preprints202603.1960.v1

2.5. High-Fidelity Aerostructural SBO Framework

The SBO framework employs high-fidelity analysis tools and is executed using five distinct DoE strategies. Following a previous study by the authors, multiple wing configurations are generated using the selected optimized airfoil [28]. The objective of the SBO framework is to identify the optimal aerostructural wing geometry that maximizes the range R, (Equation 14) of the specific aircraft, subject to constraints on the cruise lift coefficient, static strength and stiffness (global buckling).

$$R = \frac{3.6}{g} \cdot \frac{L}{D} \cdot \frac{E_{sb}\,\eta_{b2s}\,\eta_p\,m_b}{m} \tag{14}$$

where:

$$\begin{aligned} m_b &= \text{mass of batteries [kg]} \\ m &= \text{aircraft total mass [kg]} \\ E_{sb} &= \text{battery specific energy [Wh/kg]} \\ \eta_p &= \text{propeller efficiency} \\ \eta_{b2s} &= \text{total system efficiency from battery to motor output shaft} \end{aligned}$$

The optimization considers twelve key geometric design variables, comprising four aerodynamic parameters—aspect ratio, taper ratio, sweep angle, and tip twist—and eight structural parameters, including skin thickness, rib thickness, front spar thickness, rear spar thickness, rib spacing, stringer spacing, front spar location, and rear spar location. Each DoE consists of 120 wing models generated within the defined design space. Based on these samples, the SBO framework is trained and subsequently used to generate an additional 60 candidate wing configurations, with the objective of identifying the most suitable design that satisfies the imposed constraints while maximizing range. At the conclusion of each SBO iteration, an optimized wing configuration is obtained, and the resulting optimal designs from the five DoEs are finally compared to assess consistency and robustness of the optimization results. At each SBO iteration the framework starts from the generation of the geometry of the wing, the subsequent computational domain and CFD mesh. The CFD analyses are then conducted, and output is collected in terms of the lift constraint as well as the pressure field in the skins of the wing. Moving to the FEM modeling framework, interpolation schemes are used to map the pressure field from the CFD to the FEM mesh. Given the geometric parameters of the wing, Patran Command Language (PCL) scripts are used to generate a new wing geometry and mesh. Subsequently, analyses files (linear static and global buckling) are extracted and executed, followed by output collection in terms of strength and stiffness constraints. The overall flowchart of the framework is presented in Figure 7.

A summary of all variables, including their lower and upper bounds, is given in Table 3. A horizontal line is used to separate aerodynamic from structural variables. The overall optimization problem setup is summarized in Table 4.

Table 3. Optimization Variables Bounds.

Variable	Lower Bound	Upper Bound
Aspect Ratio (AR)	6.5	15
Taper Ratio (λ)	0.2	1
Quarter-chord sweep angle (Λ), deg	0°	15°
Twist (ϵ), deg	−4°	4°
Front Spar Location (FSL), $\%C$	0.15	0.3
Rear Spar Location (RSL)$\%C$	0.6	0.75
Rib Spacing (RS), $\%b/2$	0.1	0.3
Stringer Spacing (SS), $\%C$	0.1	0.3
Upper Skin Thickness (UST), mm	0.2	0.6
Lower Skin Thickness (LST), mm	0.2	0.6
Front Spar Thickness (FST), mm	0.2	0.6
Rear Spar Thickness (RST), mm	0.2	0.6
Ribs Thickness (RT), mm	0.2	0.6

 doi:10.20944/preprints202603.1960.v1

Table 4. Optimization Problem Summary.

Objective Function	**Maximize Range**
Subject to constraints	
Constraint Type	**Constraint Equation**
$C_{L_{cruise}}$ (g_1)	$0.8 - g_1 \leq 0$
FI_{max}, Shell Elements (g_2)	$g_2 - 1 \leq 0$
FoS, Beam Elements (g_3)	$1.5 - g_3 \leq 0$
Linear Buckling Eigenvalue (g_4)	$1.5 - g_4 \leq 0$

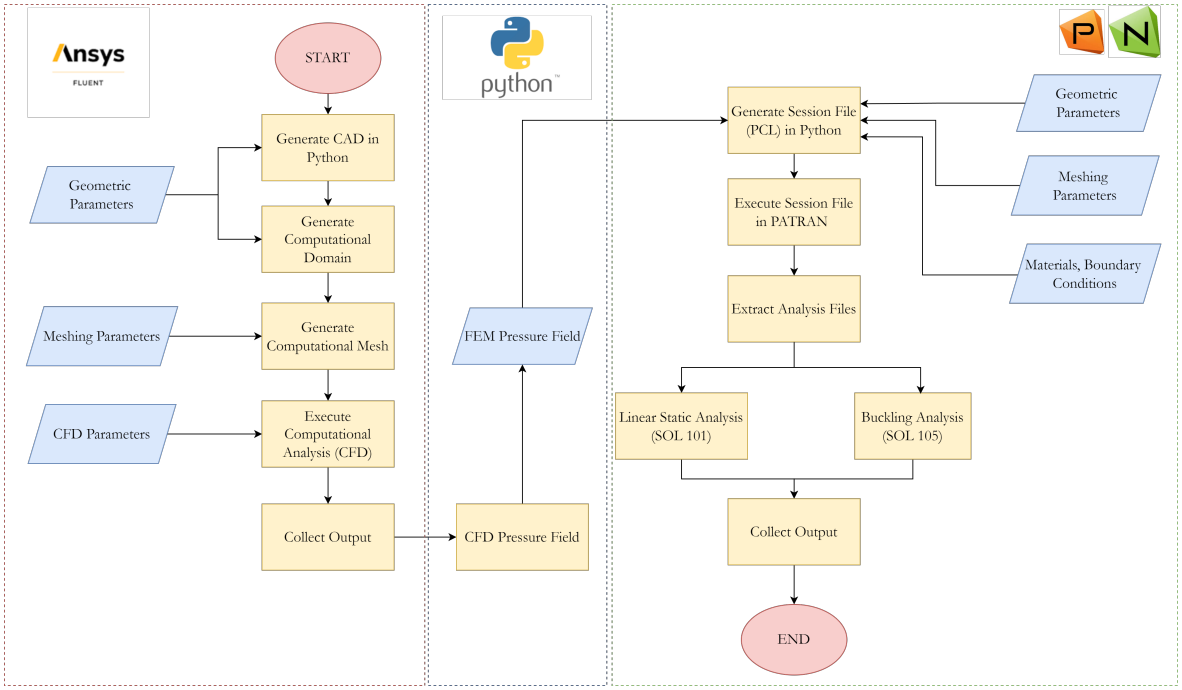

Figure 7. Parametric CFD-FEM modeling framework.

The SBO framework, as illustrated in Figure 8, is common to the previous framework and consists of two main stages: the sampling stage and the model updating stage. The process begins with the definition of the sampling size, followed by generating samples using the LHS method. Subsequently, the geometry and mesh of the geometry are generated and further analyzed via each computational tool. The objective and constraint functions are then obtained for each sample. Once the training stage is completed, the main SBO framework is initiated. The hyperparameters of the Kriging model representing the objective and constraint functions are determined. Next, the constrained expected improvement function (Equation (12)) is minimized using a sub-optimization routine, yielding a new point in the design space. The computational analysis is then performed for this new point, and the surrogate model is updated accordingly. This iterative process continues for a predefined number of infill points.

 doi:10.20944/preprints202603.1960.v1

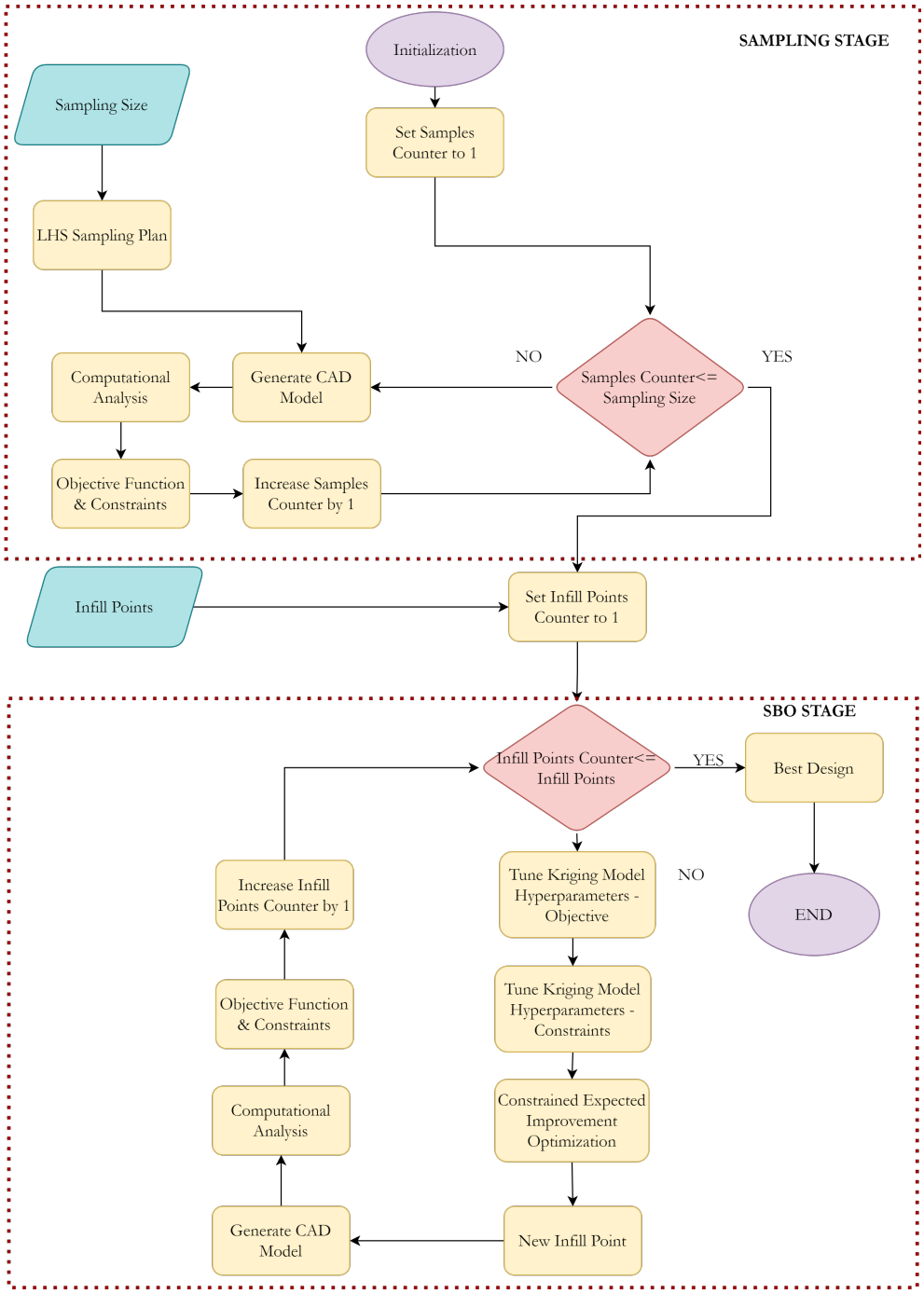

Figure 8. General SBO framework.

3. Results

3.1. Surrogate Model Accuracy

The predictive accuracy of the surrogate models was assessed using the Root Mean Square Error (RMSE) and the coefficient of determination (R^2). These metrics were evaluated using the infill points generated during the optimization process, which serve as an independent validation dataset. They quantify the average prediction error and the overall agreement between the predicted ($\hat{y}_i$) and high-fidelity (y_i) responses, and are defined as

$$\text{RMSE} = \sqrt{\frac{1}{N}\sum_{i=1}^{N}(y_i - \hat{y}_i)^2} \tag{15}$$

 doi:10.20944/preprints202603.1960.v1

$$R^2 = 1 - \frac{\sum_{i=1}^{N}(y_i - \hat{y}_i)^2}{\sum_{i=1}^{N}(y_i - \bar{y})^2} \tag{16}$$

where N denotes the number of validation points and $\bar{y}$ is the mean of the corresponding high-fidelity responses. A low RMSE and an R^2 value approaching unity indicate high predictive accuracy of the surrogate model.

The results for five independent SBO runs are summarized in Table 5.

Table 5. Surrogate model accuracy across five independent SBO runs.

Run	RMSE	R^2
1	5.658	-1.8030
2	5.972	0.9019
3	7.312	0.9225
4	4.772	0.9343
5	4.399	0.9678
Mean $\pm$ SD	5.62 ± 1.11	0.3847 ± 1.2503

Overall, the surrogate models achieved a mean RMSE of 5.62 with a standard deviation of 1.11. For four out of five runs (Runs 2–5), the coefficient of determination remains consistently high ($R^2 > 0.90$), indicating a strong correlation between the surrogate predictions and the corresponding high-fidelity responses.

In contrast, Run 1 exhibits a significantly lower R^2 value, despite having an RMSE of comparable magnitude to the other runs. This behavior is attributed to the relatively narrow range of objective function values in the corresponding infill dataset, which reduces the variance of the reference data and increases the sensitivity of the R^2 metric. As a result, even moderate absolute prediction errors lead to a disproportionately low (or negative) R^2 value. This behavior is commonly observed in surrogate-based optimization when validation points are concentrated near optimal regions. Therefore, the RMSE provides a more reliable indicator of predictive performance in this case. Considering the consistently low RMSE values across all runs, the surrogate models are shown to provide an accurate approximation of the high-fidelity response, ensuring reliable performance within the surrogate-based optimization framework.

To further evaluate the generalization capability of the surrogate model, a Leave-One-Out (LOO) cross-validation analysis was performed. In this approach, each sample in the DoE is temporarily excluded from the training set, and the model is reconstructed using the remaining $N - 1$ samples. The excluded point is then predicted, and the corresponding prediction error is recorded. This process is repeated for all N samples, providing a robust estimate of model accuracy while reducing the risk of overfitting. The LOO Root Mean Square Error ($\mathrm{RMSE}_{\mathrm{LOO}}$) is computed as

$$\mathrm{RMSE}_{\mathrm{LOO}} = \sqrt{\frac{1}{N}\sum_{i=1}^{N}(y_i - \hat{y}_{i,\mathrm{LOO}})^2} \tag{17}$$

where $\hat{y}_{i,\mathrm{LOO}}$ denotes the prediction obtained by excluding the i-th sample from the training set. In addition, the corresponding coefficient of determination, R^2_{LOO}, was also evaluated in order to quantify the overall agreement between the cross-validated predictions and the high-fidelity responses.

The computed values for the five independent SBO runs are summarized in Table 6.

 doi:10.20944/preprints202603.1960.v1

Table 6. Leave-One-Out (LOO) cross-validation accuracy of the surrogate models.

Run	max|error|	RMSE_{LOO}	R^2_{LOO}
1	2.747×10^1	7.934×10^0	0.8213
2	3.264×10^1	8.806×10^0	0.8161
3	2.746×10^1	7.833×10^0	0.8258
4	3.709×10^1	8.582×10^0	0.8112
5	2.327×10^1	8.411×10^0	0.8167
Mean $\pm$ SD	$2.959 \times 10^1 \pm 5.350 \times 10^0$	$8.313 \times 10^0 \pm 4.183 \times 10^{-1}$	0.8182 ± 0.0056

The LOO errors are highly consistent across all runs, with a mean RMSE_{LOO} of 8.31×10^0 and a mean R^2_{LOO} of 0.818 ± 0.006. The relatively small standard deviation of both metrics indicates stable surrogate behavior across the independent SBO runs. Although some isolated samples exhibit larger local deviations, as reflected by the maximum absolute errors, the overall cross-validation performance confirms that the Kriging surrogate provides a reliable approximation of the high-fidelity response throughout the sampled design space.

3.2. Best Configurations of All Five SBO Iterations

In this subsection, the best feasible configurations from each SBO iteration are presented and compared to each other. Figure 9 illustrates the convergence history of the cumulative best feasible range (R) for the five SBO iterations. Among the runs, 5^{th} SBO iteration achieves the highest final range ($\simeq$ 202.8), followed by 1^{st} iteration ($\simeq$ 196.8), whereas 2^{nd}, 3^{rd} and 4^{th} iterations converge to similar intermediate values ($\simeq 189 - 191$).

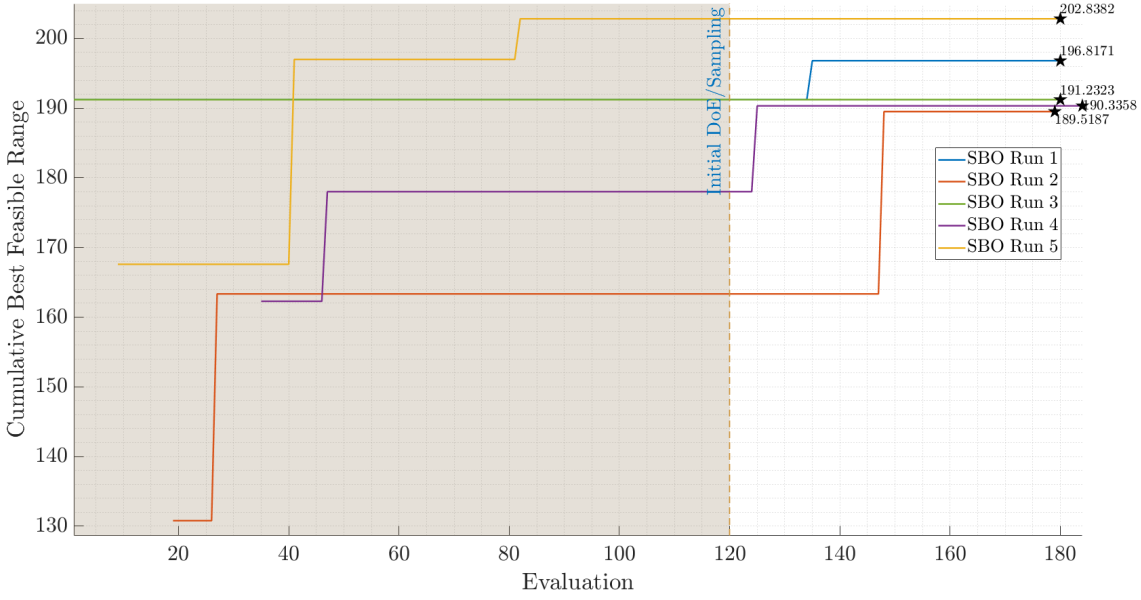

Figure 9. 1^{st} SBO iter. - Correlation between objective and constraints.

Table 7 presents the optimal configurations obtained at each SBO iteration, along with their corresponding aerodynamic and structural design parameters. All five configurations exhibit high lift-to-drag ratios ($L/D > 25.5$), while the weight remains nearly constant across all cases ($W \simeq 0.83$), indicating that performance improvements are primarily driven by aerodynamic efficiency. Regarding the constraints, g_1 and g_4 are negative and close to zero, confirming that they are active and govern the feasible boundary of the optimization. In contrast, g_2 and g_3 remain significantly negative, indicating that they are inactive and do not influence the optimal solutions. From an aerodynamic design perspective, all configurations are characterized by relatively high aspect ratios, with the fifth design achieving the largest value ($AR = 14.86$), approaching the upper bound of the design space. The

 doi:10.20944/preprints202603.1960.v1

taper ratio and sweep angle remain moderate ($\lambda < 0.44$ and $\Lambda < 10°$), while tip twist varies between $-0.40°$ and $2.11°$, reflecting adjustments in load distribution and aerodynamic performance. In terms of structural design, the parameters are generally consistent across all configurations, with the most notable variations observed in rib spacing (RS) and stringer spacing (SS), suggesting that these variables play a key role in accommodating the aerodynamic changes while maintaining structural feasibility.

Table 7. Best configurations of all iterations.

Objective and Constraints Results							
SBO Iter.	**L/D**	**W**	**R**	**g1**	**g2**	**g3**	**g4**
1	26.504	0.829	196.817	-0.021	-0.886	-1.2E+05	-0.013
2	25.518	0.828	189.519	-0.043	-0.882	-2.2E+05	-0.099
3	25.752	0.829	191.232	-0.004	-0.887	-1.7E+05	-0.192
4	25.642	0.832	190.336	-0.024	-0.897	-1.0E+05	-0.240
5	27.292	0.823	202.838	-0.023	-0.877	-2.2E+05	-0.075

Aerodynamic Design Parameters				
SBO Iter.	**AR**	λ	Λ	ε
1	13.93	0.22	3.55	-0.40
2	12.63	0.34	2.29	2.11
3	12.83	0.28	5.76	0.31
4	13.09	0.23	0.90	1.48
5	14.86	0.44	8.85	0.06

Structural Design Parameters								
SBO Iter.	**FSL**	**RSL**	**RS**	**SS**	**UST**	**LST**	**RST**	**RT**
1	0.279	0.662	0.258	0.186	0.00052	0.00040	0.00050	0.00043
2	0.291	0.645	0.242	0.264	0.00052	0.00024	0.00050	0.00052
3	0.267	0.609	0.245	0.155	0.00049	0.00055	0.00057	0.00031
4	0.262	0.666	0.156	0.121	0.00053	0.00041	0.00036	0.00023
5	0.255	0.678	0.120	0.287	0.00044	0.00050	0.00057	0.00031

Figure 10 illustrates the planform geometry of the five best wing configurations, including their key dimensions: semi-span ($b/2$), root chord (C_{root}), and tip chord (C_{tip}), but also the ribs, spars (grey lines) and stringers (grey dashed lines). Figure 11 presents the corresponding aerodynamic performance obtained from CFD analyses, including the variations of lift coefficient (C_L), drag coefficient (C_D), moment coefficient (C_m), and lift-to-drag ratio (L/D) with angle of attack (AoA). Among the configurations, the 5th wing demonstrates the best overall aerodynamic performance. It achieves the highest lift-to-drag ratio and maintains superior behavior across the entire AoA range, indicating improved aerodynamic efficiency and stability characteristics compared to the other designs.

Therefore, the 5^{th} wing configuration is selected as the optimal design, as it demonstrates superior performance among the five candidates. It achieves the maximum range of $\simeq 203km$ while also exhibiting the best overall aerodynamic characteristics. In addition, it satisfies all the constraints imposed in the SBO optimization process.

 doi:10.20944/preprints202603.1960.v1

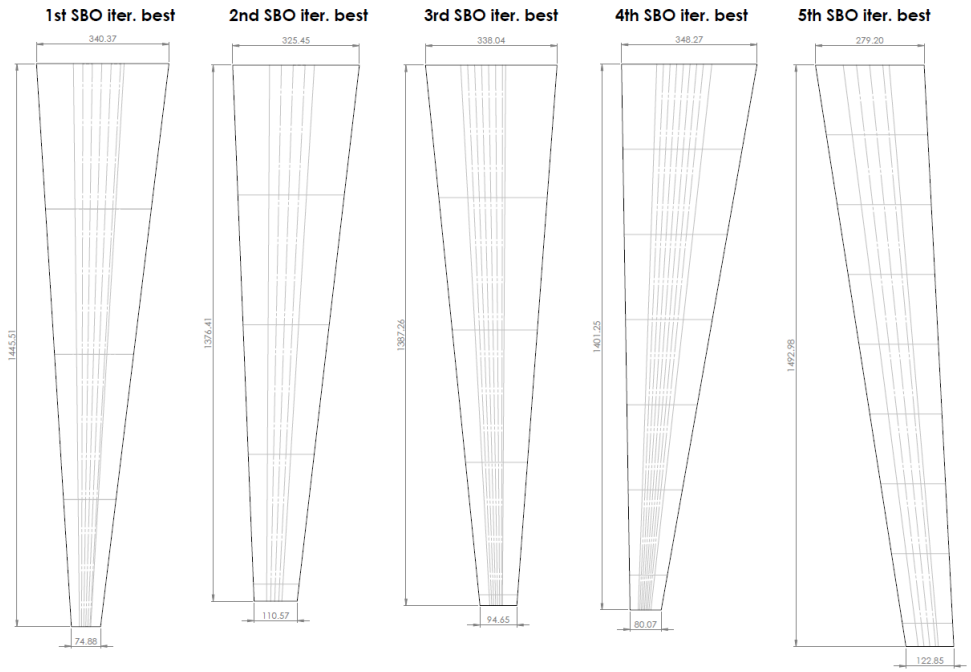

Figure 10. 1^{st} SBO iter. - Correlation between objective and constraints.

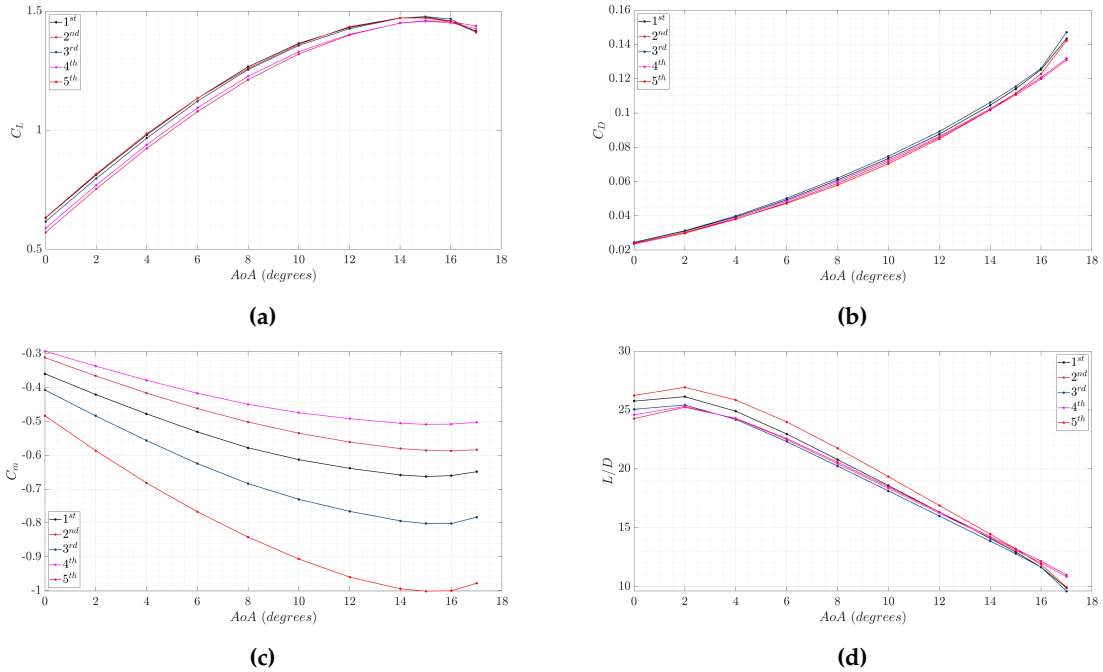

Figure 11. CFD Aerodynamic results for each best wing configuration of the 5 SBO iterations - C_L(**a**), C_D(**b**), C_m (**c**), and L/D(**d**) vs AoA.

3.3. Selected Optimized Configuration

In this subsection, the results of the 5^{th} SBO iteration are presented, from which the best optimized wing configuration was selected. In addition, the results of the aerodynamic and structural analyses of the optimized wing are presented. Figure 12 presents the correlation matrix for the final dataset after incorporating all samples and infill points, providing a consolidated view of the relationships among the performance variables and constraints. As observed in all previous iterations (Figures A1, A5, A9 and A13), L/D and R maintain a nearly perfect positive correlation (0.99), confirming that aerodynamic efficiency consistently dominates range performance throughout the optimization process. The correlation between weight and the performance variables remains weakly negative, with W showing correlations of- 0.05 with L/D and -0.18 with R, indicating that, within the explored design space,

 doi:10.20944/preprints202603.1960.v1

variations in weight have a relatively limited influence on range compared to aerodynamic efficiency. The constraint correlations remain generally weak with respect to the primary performance variables. Constraint g_1 shows almost no correlation with L/D(0.01) and R(0.04), while maintaining a modest negative correlation with weight (-0.25), suggesting limited coupling with the main design variables. Constraint g_2 exhibits slightly stronger positive correlations with L/D(0.30) and R(0.33), indicating a mild dependence on aerodynamic performance, while g_3 continues to show weak correlations with all variables. Among the constraints, g_4 remains the most strongly influenced by the design variables, displaying a moderate negative correlation with weight (-0.65) and moderate positive correlations with R(0.29) and g_2(0.64). Overall, the final correlation structure confirms that aerodynamic efficiency is the primary driver of range, while most constraints remain weakly coupled to the performance variables, with g_4 showing the most noticeable dependency within the constraint set.

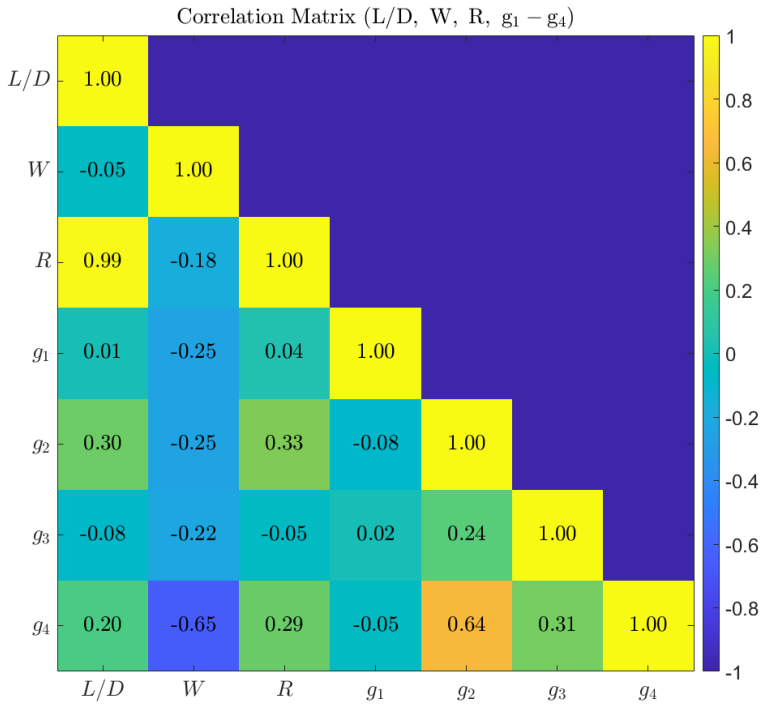

Figure 12. 5^{th} SBO iter. - Correlation between objective and constraints.

Figure 13 presents the correlation between wing design variables and range R for the fifth and final iteration, reflecting the fully converged design space. Consistent with all previous iterations (Figures A2, A6, A10 and A14), the aspect ratio remains the dominant driver of range, exhibiting a very strong positive correlation ($\simeq 0.94$). The tip twist also maintains a moderate positive correlation ($\simeq 0.43$), reinforcing its role as the most influential secondary aerodynamic variable. In contrast, the taper ratio continues to show a moderate negative correlation ($\simeq -0.30$), while the sweep angle retains only a weak negative influence, confirming its limited impact on range. The influence of structural variables becomes more clearly defined but remains relatively secondary compared to aerodynamic parameters. Stringer spacing shows a small positive correlation, while rib spacing and front spar location exhibit only weak positive effects. On the other hand, several structural variables display consistent negative correlations with range, most notably rear spar location ($\simeq -0.22$), skin thickness ($\simeq -0.27$), rear spar thickness ($\simeq -0.10$), and rib thickness ($\simeq -0.14$). These trends suggest that increases in structural thickness and certain placement parameters tend to reduce range, likely due to associated weight penalties. Overall, the final iteration confirms a stable and well-defined relationship structure: aerodynamic variables—particularly aspect ratio and tip twist—dominate range performance, while structural variables exert smaller, mostly negative influences. This indicates that, at convergence, the optimization has clearly identified the primary performance drivers and reduced uncertainty in the role of secondary design variables.

 doi:10.20944/preprints202603.1960.v1

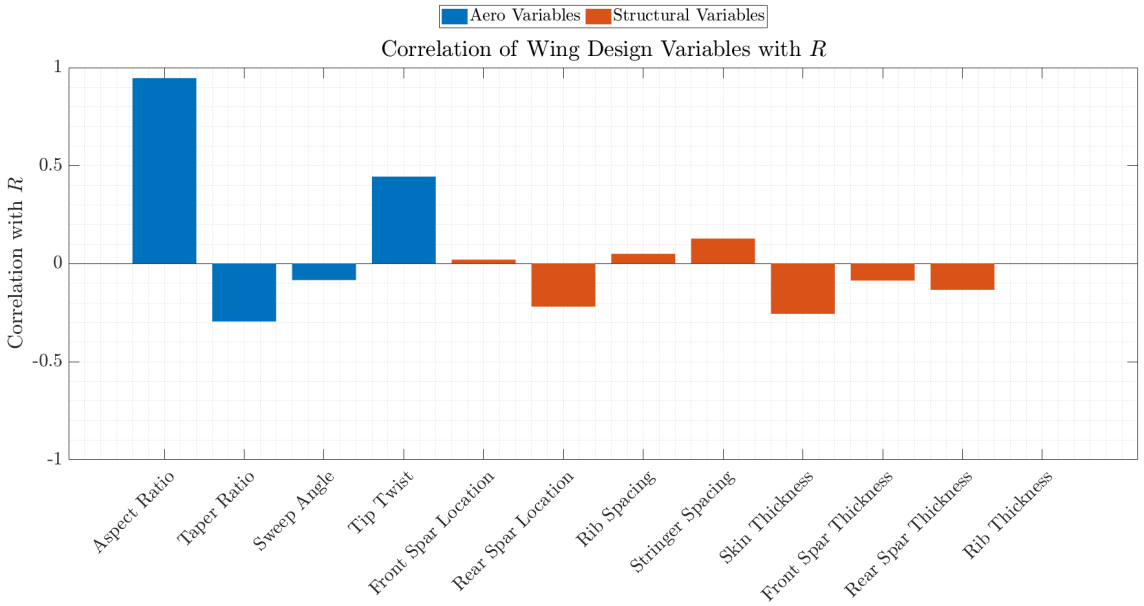

Figure 13. 5^{th} SBO iter. - Correlation of aerodynamic and structural design parameters with Range-Objective.

Figure 14 shows the correlation of aerodynamic and structural design variables with L/D(a) and weight W(b) for the 5^{th} SBO iteration, reflecting the fully converged relationships in the design space. For L/D(Figure 14-a), the aspect ratio remains the dominant parameter, exhibiting a consistently strong positive correlation ($\simeq$ 0.95). The tip twist retains a moderate positive correlation ($\simeq$ 0.4), confirming its role as the most influential secondary aerodynamic variable. The taper ratio continues to show a moderate negative correlation, while the sweep angle has only a weak negative effect. Compared to earlier iterations, the influence of structural variables on L/D is minimal. Most structural parameters cluster close to zero, with only small negative correlations observed for rear spar location, skin thickness, and spar thicknesses, indicating a weak detrimental effect on aerodynamic efficiency. For weight W(14-b), structural variables clearly dominate. Skin thickness maintains a very strong positive correlation ($\simeq$ 0.85), confirming it as the primary driver of weight. Other structural variables, such as front spar location, rib spacing, and stringer spacing, show small negative correlations, while spar thicknesses and rib thickness exhibit weak positive or near-zero effects. Aerodynamic variables have negligible influence on weight, with correlations remaining close to zero or weakly negative. Overall, the final iteration demonstrates a well-converged and decoupled relationship structure, where L/D is governed almost entirely by aerodynamic variables (primarily aspect ratio and tip twist), and weight is dominated by structural thickness—especially skin thickness—with minimal cross-coupling between aerodynamic and structural design variables.

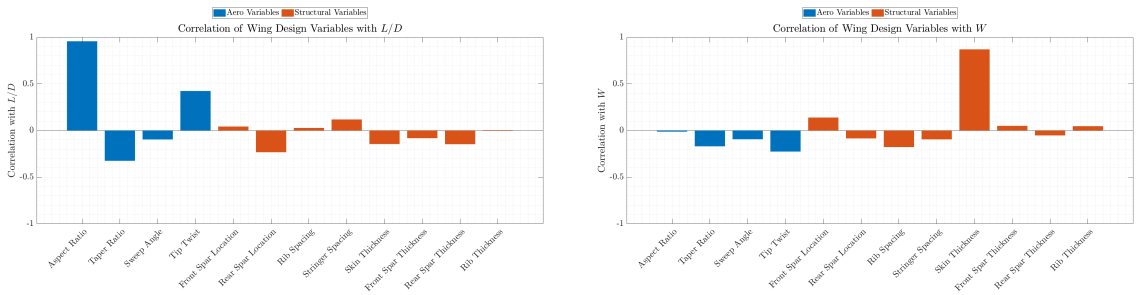

(a) **(b)**

Figure 14. 5^{th} SBO iter. - Correlation of aerodynamic and structural design parameters with L/D (**a**), and *Weight* (**b**).

Figure 15 presents the correlation of aerodynamic and structural design variables with the constraint functions g_1, g_2, g_3 and g_4 for the 5^{th} SBO iteration, reflecting the fully converged con-

 doi:10.20944/preprints202603.1960.v1

straint–design relationships. As in previous iterations (Figures A4, A8, A12 and A16), all constraints are defined such that $g_i < 0$ corresponds to feasible designs; thus, negative correlations indicate improved constraint satisfaction, while positive correlations indicate a tendency toward violation.

For g_1(Figure 15-a), tip twist remains the dominant variable, exhibiting a strong positive correlation, confirming that increasing twist drives the design toward violating this constraint. Aspect ratio shows a weak negative correlation, indicating a slight improvement in feasibility with increasing aspect ratio. Structural variables exhibit minimal influence, with only very small correlations, suggesting that g_1 is primarily governed by aerodynamic variables at convergence.

For g_2(Figure 15-b), a clearer aerodynamic influence emerges. Aspect ratio, taper ratio, and sweep angle show moderate positive correlations, indicating that increasing these parameters tends to reduce feasibility. In contrast, structural variables show mixed but generally weak effects, with front spar location exhibiting a noticeable negative correlation, suggesting a potential role in improving constraint satisfaction.

For g_3(Figure 15-c), the correlations remain relatively weak overall. Aerodynamic variables show small positive correlations, while structural variables display mixed behavior. Rear spar location and front spar thickness show positive correlations, whereas skin thickness and rib thickness show negative correlations, indicating that increasing structural thickness helps satisfy this constraint.

For g_4(Figure 15-d), the strongest and most consistent relationships are observed. Aerodynamic variables—particularly aspect ratio, taper ratio, and sweep angle—show moderate positive correlations, indicating that improvements in aerodynamic performance tend to push the design toward constraint violation. In contrast, skin thickness exhibits a strong negative correlation, with additional negative contributions from spar thicknesses and rib thickness, confirming that structural sizing remains the primary mechanism for restoring feasibility.

Overall, the final iteration demonstrates a well-defined and decoupled constraint structure: g_1 and g_2 are primarily influenced by aerodynamic variables, g_3 shows weak and mixed sensitivity, and g_4 remains the most critical constraint, governed by a balance between aerodynamic drivers (causing violation) and structural thickness variables (ensuring feasibility).

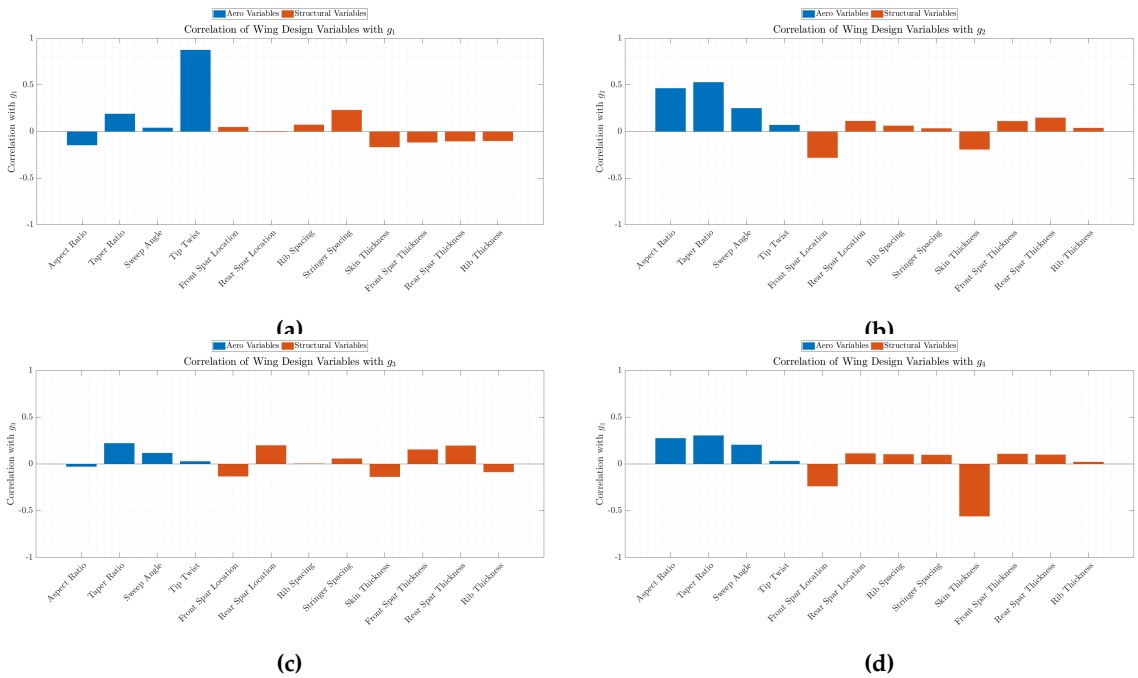

Figure 15. 5^{th} SBO iter. - Correlation of aerodynamic and structural design parameters with g_1 (**a**), g_2 (**b**), g_3 (**c**), and g_4 (**d**).

Tables 8 and 9 show the feasible designs of the 5^{th} SBO iteration, for both samples and infills, respectively. Constraints g_1 and g_4 remain close to zero for the feasible configurations, indicating

 doi:10.20944/preprints202603.1960.v1

that they primarily govern the optimal solutions. In contrast, g_2 and g_3 exhibit significantly negative values across all configurations, suggesting that they are inactive and do not restrict the optimization. The most feasible designs are characterized by by a high lift-to-drag ratio values and a relatively narrow range of weight, confirming that improvements in aerodynamic efficiency drive the range optimization. The infill results further demonstrate convergence towards a well-defined region of the design space. Overall, this indicates that the optimization successfully identifies feasible, high-performance configurations, where the trade-off between maximizing range and satisfying the most critical constraints - g_1 and g_4 - defines the optimal design boundaries.

Table 8. SBO 5^{th} iteration - Best possible configurations results of Samples.

A/A	L/D	W	R	g_1	g_2	g_3	g_4
			Samples				
9	22.622	0.846	167.593	-0.008	-0.928	-2.9E+05	-0.437
23	19.552	0.773	146.341	-0.024	-0.889	-1.8E+05	-0.042
26	18.796	0.802	140.103	-0.022	-0.826	-3.8E+05	-0.077
42	26.463	0.811	197.000	-0.043	-0.913	-5.1E+05	-0.811
49	25.901	0.813	192.770	-0.056	-0.880	-6.6E+05	-0.077
50	24.273	0.782	181.443	-0.074	-0.909	-5.1E+06	-0.488
58	20.340	0.796	151.737	-0.013	-0.871	-2.6E+05	-0.025
60	18.499	0.805	137.829	-0.041	-0.918	-5.3E+05	-0.699
66	25.761	0.808	191.868	-0.025	-0.851	-1.8E+06	-0.289
70	17.826	0.794	133.026	-0.042	-0.938	-3.7E+05	-1.268
78	24.981	0.814	185.914	-0.038	-0.915	-8.7E+05	-0.789
83	27.292	0.823	202.838	-0.023	-0.877	-2.2E+05	-0.075
87	24.456	0.846	181.177	-0.002	-0.897	-2.2E+05	-0.220

Table 9. SBO 5^{th} iteration - Best possible configurations results of Infills.

A/A	L/D	W	R	g_1	g_2	g_3	g_4
			Infills				
2	17.713	0.814	131.807	-0.035	-0.900	-1.9E+05	-0.164
6	17.799	0.800	132.723	-0.037	-0.896	-1.7E+05	-0.098
8	17.767	0.812	132.241	-0.034	-0.861	-4.0E+05	-0.009
9	24.289	0.814	180.752	-0.040	-0.892	-2.2E+05	-0.168
10	17.556	0.802	130.875	-0.046	-0.892	-1.4E+05	-0.085
13	17.395	0.811	129.499	-0.041	-0.862	-2.3E+05	-0.039
14	17.948	0.799	133.838	-0.032	-0.896	-1.5E+05	-0.097
17	24.817	0.813	184.707	-0.047	-0.885	-2.0E+05	-0.094
18	22.614	0.829	167.938	-0.008	-0.925	-9.5E+05	-0.523
19	22.588	0.824	167.851	-0.018	-0.917	-8.7E+05	-0.417
23	22.596	0.825	167.897	-0.015	-0.920	-8.3E+06	-0.420
25	22.601	0.826	167.913	-0.012	-0.922	-2.3E+06	-0.458
34	23.095	0.797	172.268	-0.047	-0.893	-2.6E+05	-0.036
35	16.799	0.799	125.275	-0.011	-0.906	-4.3E+05	-0.228
36	17.652	0.792	131.760	-0.040	-0.931	-5.4E+05	-1.055
37	22.671	0.823	168.493	-0.003	-0.918	-9.3E+05	-0.360
38	22.668	0.823	168.469	-0.003	-0.918	-8.7E+05	-0.340
39	23.108	0.809	172.076	-0.031	-0.892	-1.3E+06	-0.032
40	22.766	0.823	169.202	-0.009	-0.914	-2.4E+05	-0.349
41	23.113	0.809	172.115	-0.030	-0.892	-4.3E+05	-0.024
42	22.816	0.817	169.719	-0.009	-0.914	-5.0E+05	-0.197
43	22.764	0.823	169.175	-0.009	-0.914	-1.7E+06	-0.349
44	22.785	0.819	169.443	-0.009	-0.915	-6.1E+05	-0.354
45	23.082	0.810	171.870	-0.030	-0.894	-6.9E+05	-0.050
46	23.056	0.810	171.674	-0.029	-0.894	-4.1E+05	-0.048
47	22.800	0.818	169.571	-0.010	-0.915	-5.9E+05	-0.300
48	23.078	0.810	171.840	-0.029	-0.894	-7.9E+05	-0.054
56	22.794	0.818	169.537	-0.009	-0.914	-6.3E+05	-0.345
58	23.217	0.809	172.894	-0.032	-0.930	-3.8E+05	-1.077
60	17.744	0.799	132.318	-0.044	-0.893	-3.2E+05	-0.008

 doi:10.20944/preprints202603.1960.v1

3.3.1. Aerostructural Analysis of the Best Configuration

This subsection presents the aerodynamic analysis results obtained at an angle of attack of 12°, which were used as the basis for the FEM analyses. Figure 16 illustrates the contours of the Y^+ distribution over the upper and lower surfaces of the selected wing configuration, where the values range from 0 to 3.24.

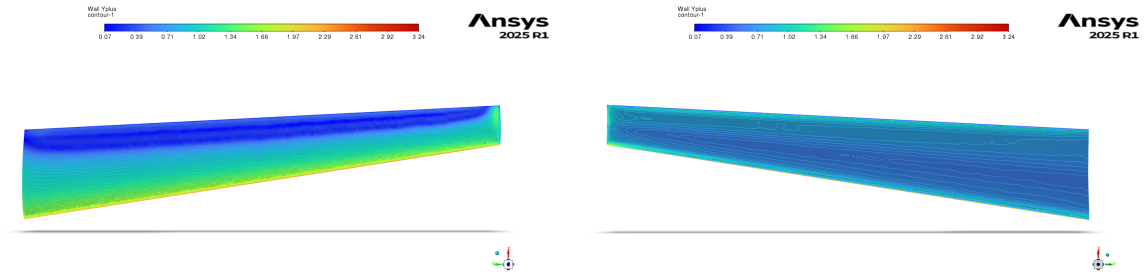

(a) **(b)**

Figure 16. Y^+ contours on upper (**a**), and lower (**b**) wing surfaces of the selected optimized configuration.

Figure 17 presents the pressure coefficient and temperature contours on the upper wing surface obtained from the aerodynamic analysis at 12° AoA. A minor flow separation is observed near the trailing edge, along with a small vortex forming at the wing tip.

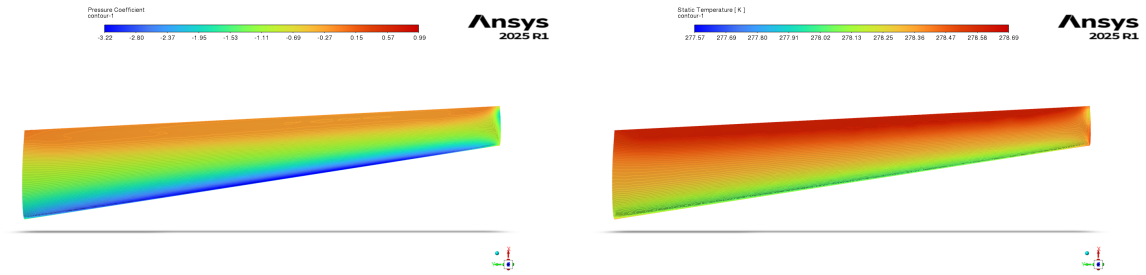

(a) **(b)**

Figure 17. Pressure coefficient (**a**), and temperature (**b**) contours of surfaces of the selected optimized configuration.

The previously discussed flow detachment is more clearly demonstrated in Figure 18, which presents the airflow pathlines for the examined case. In Figures 18-(b) and (d), a small vortex forms near the trailing edge, characterized by flow rotation about the y-axis, resulting in localized flow separation. Additionally, Figure 18-(c) provides a clearer view of the tip vortex.

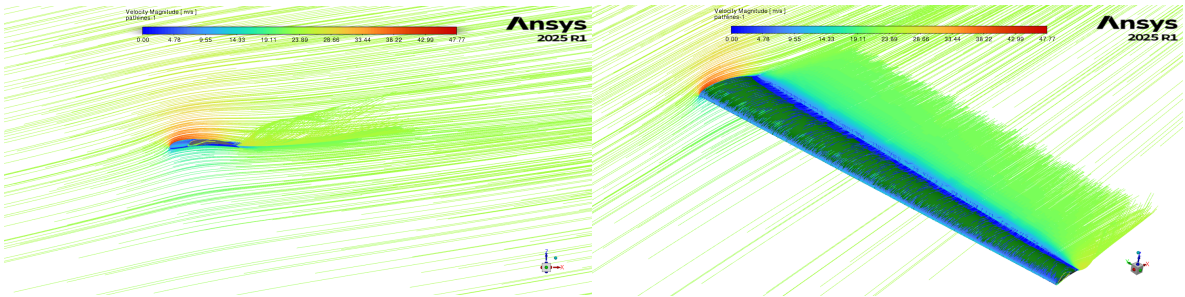

(a) **(b)**

Figure 18. *Cont.*

 doi:10.20944/preprints202603.1960.v1

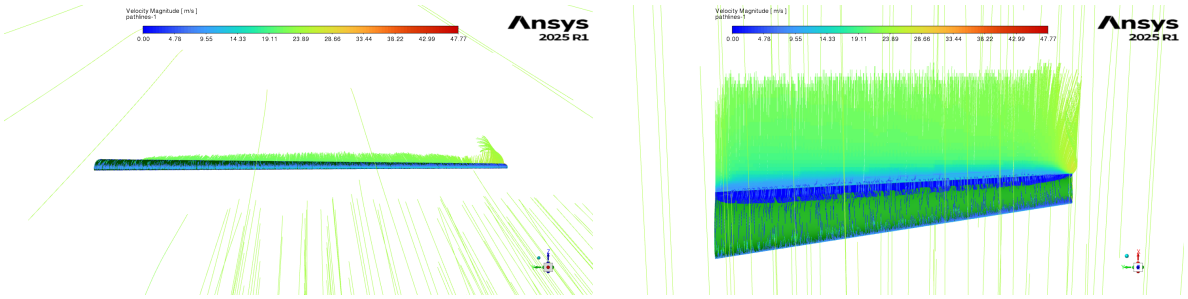

(c) (d)

Figure 18. Velocity pathlines around the wing of the selected optimized configuration.

The structural response of the optimal wing configuration is also examined, providing important insight in the structural behavior of the optimized design and confirm the effectiveness of the proposed aerostructural optimization framework. In particular, Figure 19 illustrates the displacement field of the wing under aerodynamic loading. The deformation pattern is dominated by bending, with maximum deflection occurring at the wing tip, which is consistent with typical cantilever wing behavior. The magnitude of deformation remains within acceptable limits, ensuring that aerodynamic performance is not significantly degraded due to excessive aeroelastic effects. This result further demonstrates that the optimized design achieves a suitable compromise between structural flexibility and stiffness.

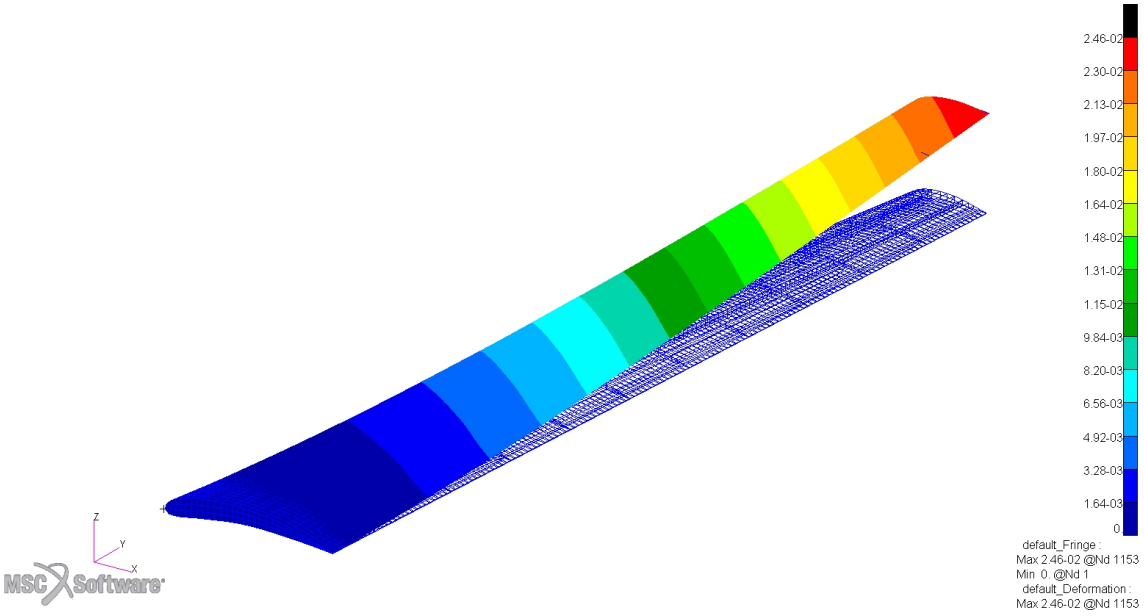

Figure 19. Deformed shape contour (m) of the selected optimized configuration.

The distribution of the maximum failure index across the wing structure is also presented in Figure 20. The highest values are observed near the wing root region, where bending moments are largest due to aerodynamic loading. Despite these localized peaks, the maximum failure index remains below the allowable limit, confirming that the optimized structure satisfies the strength constraints. A similar trend is observed for the maximum beam stress distribution within the structural members (Figure 21). Elevated stress levels are again concentrated near the wing root and along primary load-carrying components such as spars, reflecting the load transfer mechanism within the wing. The stress distribution is smooth and does not exhibit abrupt concentrations, suggesting that the structural layout and sizing variables have been appropriately tuned during the optimization process. The absence of excessive stress peaks further confirms that the design achieves an efficient balance between weight minimization and structural integrity. Overall, the structural response of the optimal configuration demonstrates that the proposed SBO framework successfully captures the interaction between aerodynamic loading and structural behavior. The results confirm that structural variables,

 doi:10.20944/preprints202603.1960.v1

particularly skin thickness and internal layout parameters, are actively driven by strength and stability constraints, while aerodynamic variables govern performance. This interplay leads to a structurally efficient and aerodynamically optimized wing design.

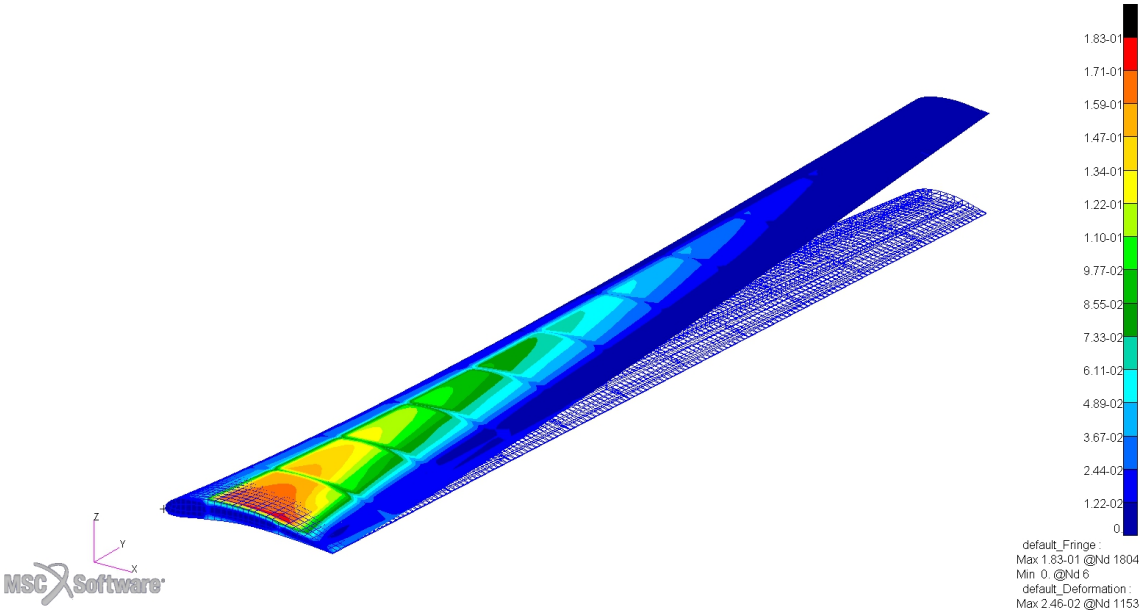

Figure 20. Maximum FI contour of the selected optimized configuration.

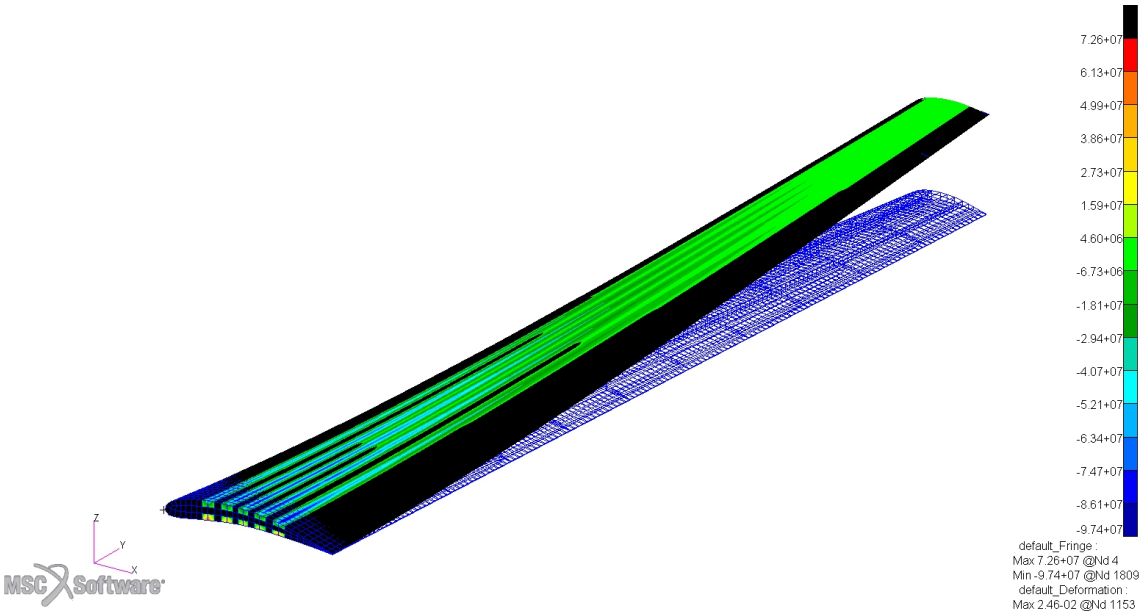

Figure 21. Maximum beam stresses contour (MPa) of the selected optimized configuration.

4. Discussion and Conclusions

This study presented a coupled aerostructural optimization framework for the preliminary design of a low-Reynolds-number composite UAV wing, integrating high-fidelity Computational Fluid Dynamics (CFD) and Finite Element Method (FEM) analyses within a surrogate-based optimization (SBO) approach. The methodology enabled efficient exploration of a multidisciplinary design space, combining aerodynamic planform variables with structural sizing parameters, while significantly reducing the computational cost associated with repeated high-fidelity simulations.

The results demonstrated that the proposed SBO framework is capable of consistently converging toward feasible high-performance solutions across multiple independent optimization runs. The

 doi:10.20944/preprints202603.1960.v1

surrogate models exhibited strong predictive capability, as confirmed by RMSE and Leave-One-Out validation metrics, ensuring reliable approximation of the underlying high-fidelity responses throughout the optimization process.

From a design perspective, the results revealed a clear separation of roles among the design variables. Aerodynamic parameters, particularly aspect ratio and tip twist, were identified as the primary drivers of range performance due to their direct influence on lift-to-drag ratio. In contrast, structural variables—most notably skin thickness—played a critical role in satisfying strength and buckling constraints, thereby defining the feasible design space. The optimal solutions emerged from the interaction between performance-driven aerodynamic variables and constraint-driven structural sizing, highlighting the importance of properly accounting for aerostructural coupling even in preliminary design stages.

The optimal wing configuration achieved a maximum range of approximately 203 km while satisfying all aerodynamic and structural constraints, demonstrating the effectiveness of the proposed framework for early-stage UAV design. Furthermore, the consistency of the results across different Design of Experiments (DoE) strategies indicates robustness with respect to initial sampling, reinforcing the reliability of the SBO approach.

Despite these promising results, several limitations remain. The present study relies on steady RANS simulations and linear structural analysis, which may not fully capture unsteady aerodynamic effects or geometric nonlinearities in highly flexible wings. Additionally, uncertainties related to material properties, manufacturing tolerances, and operational conditions were not considered in the optimization process.

Future work will focus on extending the proposed framework to address these limitations. In particular, the incorporation of geometrically nonlinear structural models and unsteady aerodynamic simulations would enable more accurate prediction of aeroelastic behavior. The integration of uncertainty quantification and reliability-based design optimization (RBDO) techniques represents another important direction, allowing for more robust and realistic design solutions. Furthermore, the application of multi-fidelity strategies could further improve computational efficiency by combining low- and high-fidelity models within the SBO framework. Finally, the extension of the methodology to full aircraft configurations, including fuselage and tail interactions, would provide a more comprehensive assessment of overall aircraft performance.

Overall, the proposed aerostructural SBO framework provides a robust and efficient tool for the preliminary design of low-Reynolds-number UAV wings, bridging the gap between high-fidelity analysis and computationally tractable optimization.

Author Contributions: Conceptualization, E.N. and S.K.; methodology, E.N. and S.K.; software, E.N., S.K. and P.K.; validation, E.N., S.K. and P.K.; formal analysis, E.N. and S.K.; investigation, E.N. and S.K.; resources, E.N., S.K. and P.K.; data curation, E.N., S.K. and P.K.; writing—original draft preparation, E.N. and S.K.; writing—review and editing, E.N. and S.K.; visualization, E.N. and S.K.; supervision, S.K., P.K., V.L., and V.K.; project administration, E.N., S.K., V.L. and V.K. All authors have read and agreed to the published version of the manuscript.

Funding: This research received no external funding.

Institutional Review Board Statement: Not applicable.

Informed Consent Statement: Not applicable.

Data Availability Statement: Data are available on request.

Conflicts of Interest: The authors declare no conflict of interest.

 doi:10.20944/preprints202603.1960.v1

Abbreviations

The following abbreviations are used in this manuscript:

AoA	Angle of Attack
ASL	Above Sea Level
CFD	Computational Fluid Dynamics
DoE	Design of Experiments
DoF	Degrees of Freedom
EI	Expected Improvement
FEM	Finite Element Method
FVM	Finite Volume Method
LHS	Latin Hypercube Sampling
LOO	Leave-One-Out
MAC	Mean Aerodynamic Chord
MSE	Mean Squared Error
RANS	Reynolds Averaged Navier Stokes
RMSE	Root Mean Square Error
SBO	Surrogate Based Optimization
SL	Sea Level
UAV	Unmanned Aerial Vehicle

Appendix A

Appendix A.1. 1^{st} *Iteration*

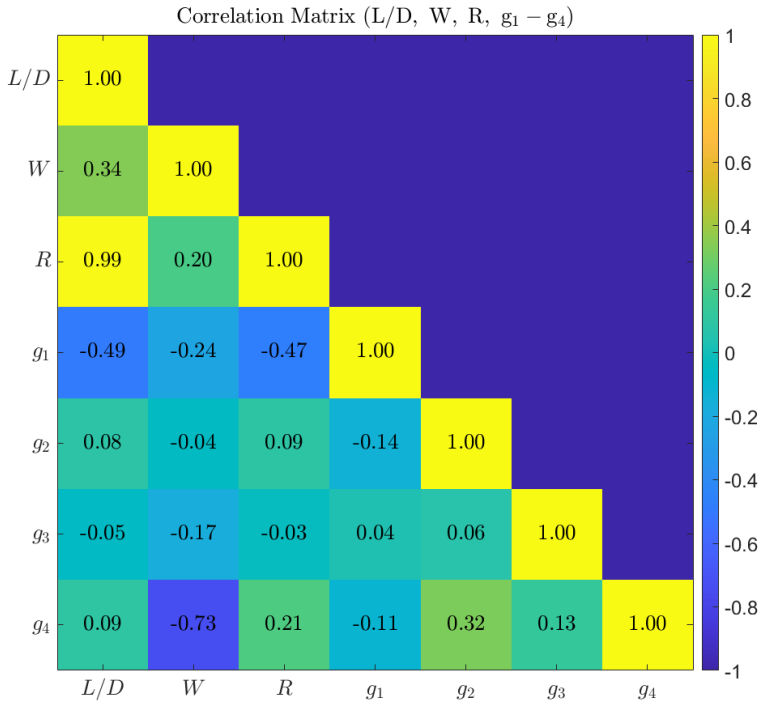

Figure A1. 1^{st} SBO iter. - Correlation between objective and constraints

 doi:10.20944/preprints202603.1960.v1

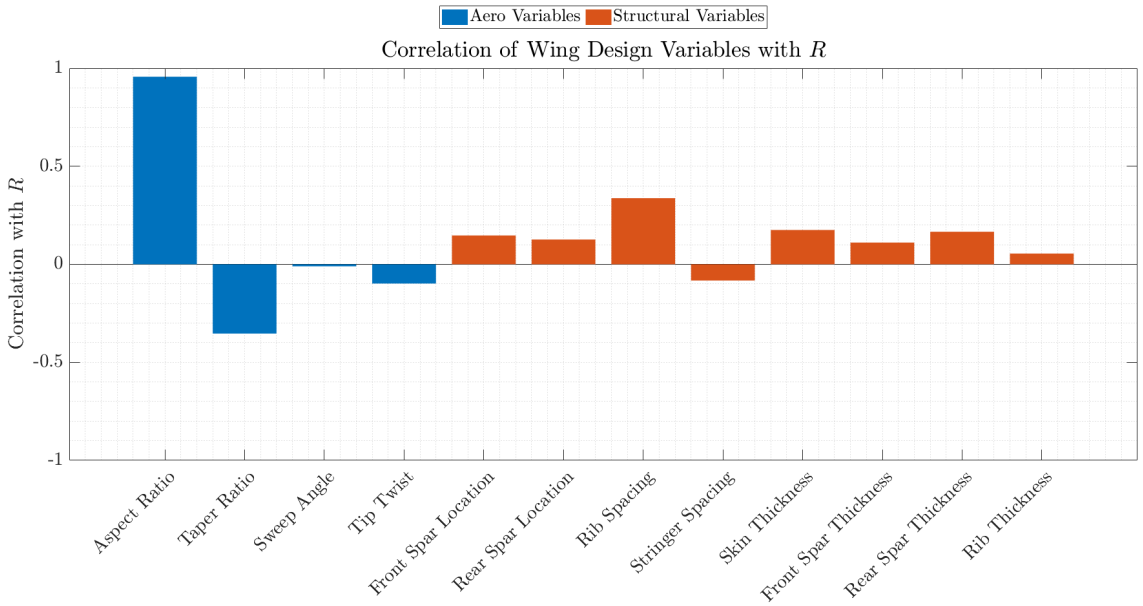

Figure A2. 1^{st} SBO iter. - Correlation of aerodynamic and structural design parameters with Range-Objective

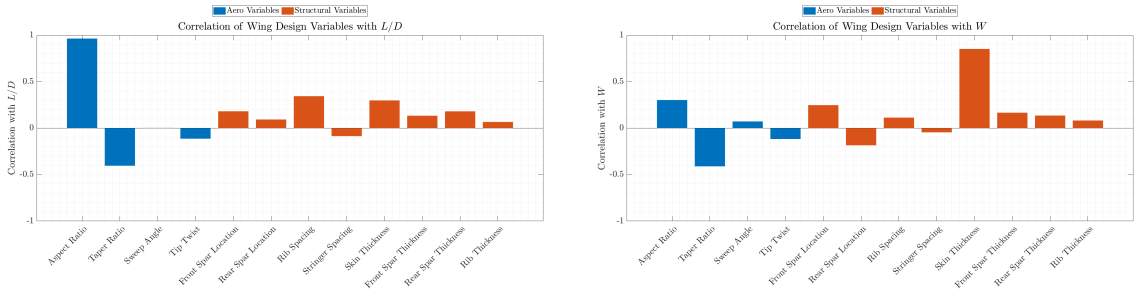

(a) **(b)**

Figure A3. 1^{st} SBO iter. - Correlation of aerodynamic and structural design parameters with L/D (**a**), and *Weight* (**b**).

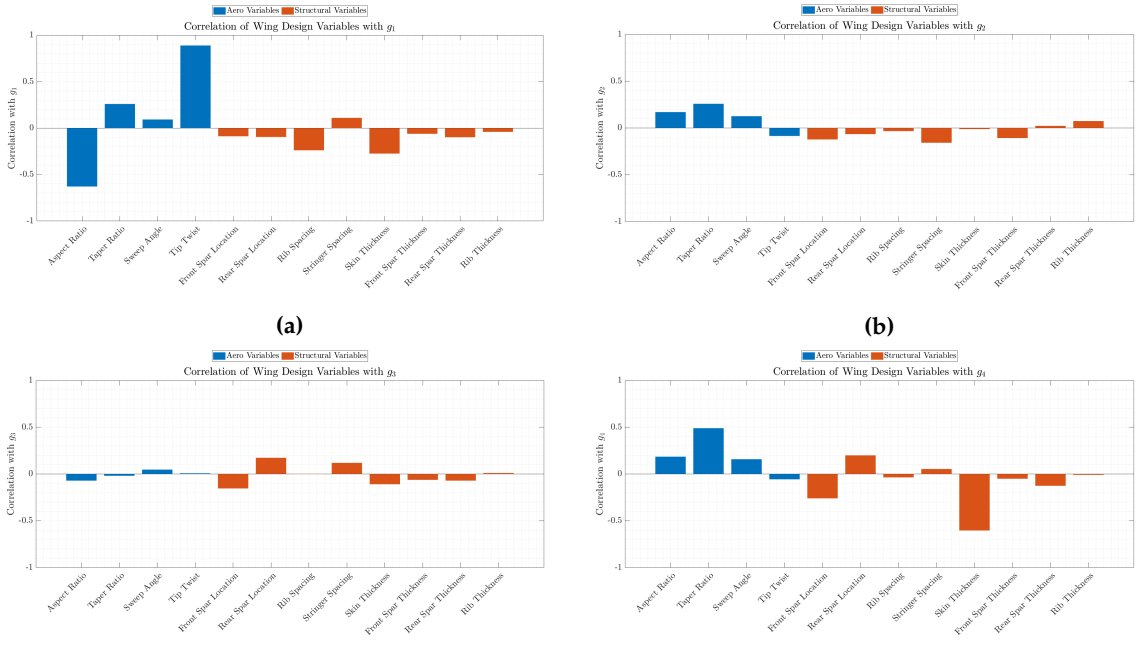

(a) **(b)**

(c) **(d)**

Figure A4. 1^{st} SBO iter. - Correlation of aerodynamic and structural design parameters with g_1 (**a**), g_2 (**b**), g_3 (**c**), and g_4 (**d**).

 doi:10.20944/preprints202603.1960.v1

Appendix A.2. 2nd DoE

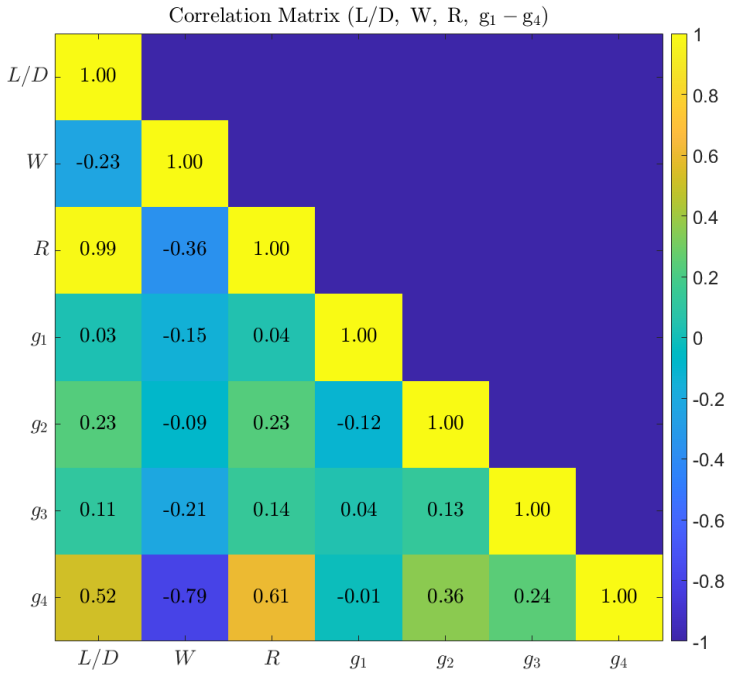

Figure A5. 2nd SBO iter. - Correlation between objective and constraints.

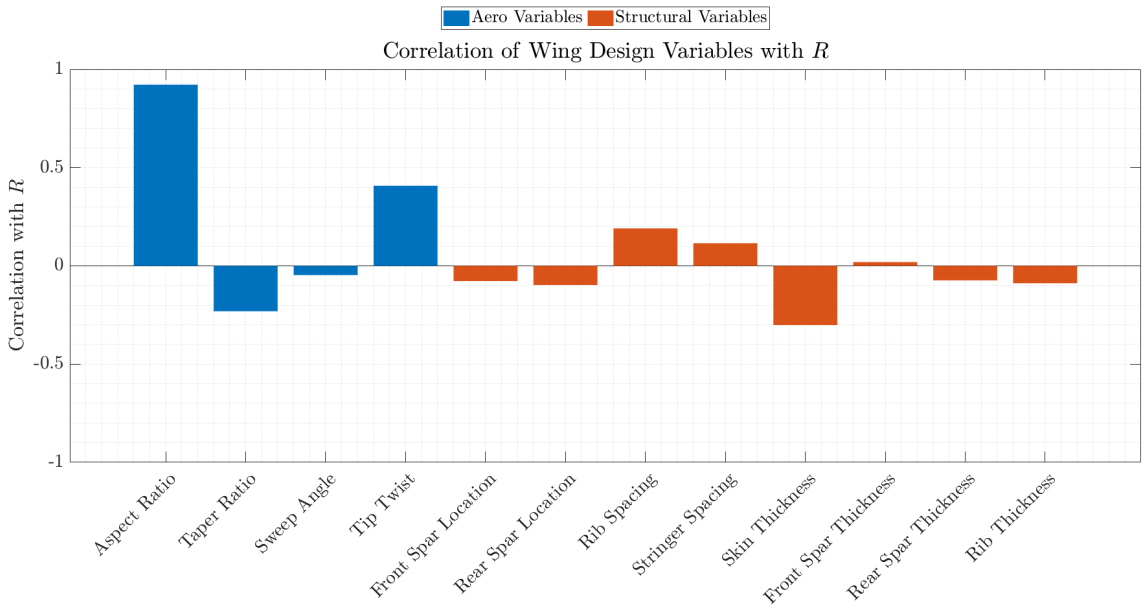

Figure A6. 2nd SBO iter. - Correlation of aerodynamic and structural design parameters with Range-Objective.

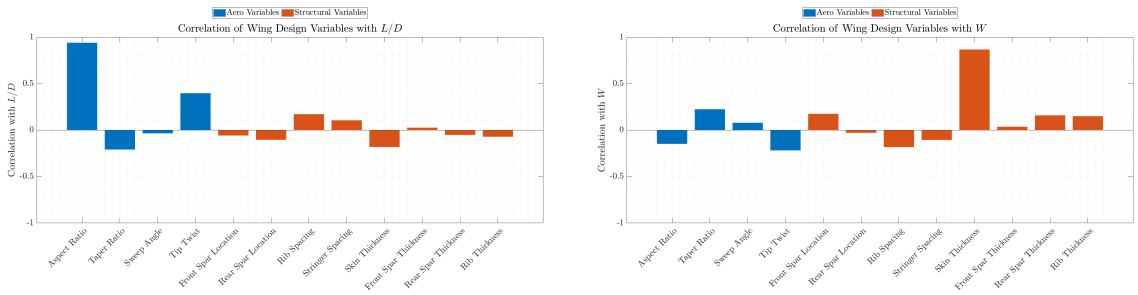

(a) **(b)**

Figure A7. 2nd SBO iter. - Correlation of aerodynamic and structural design parameters with L/D (**a**), and *Weight* (**b**).

 doi:10.20944/preprints202603.1960.v1

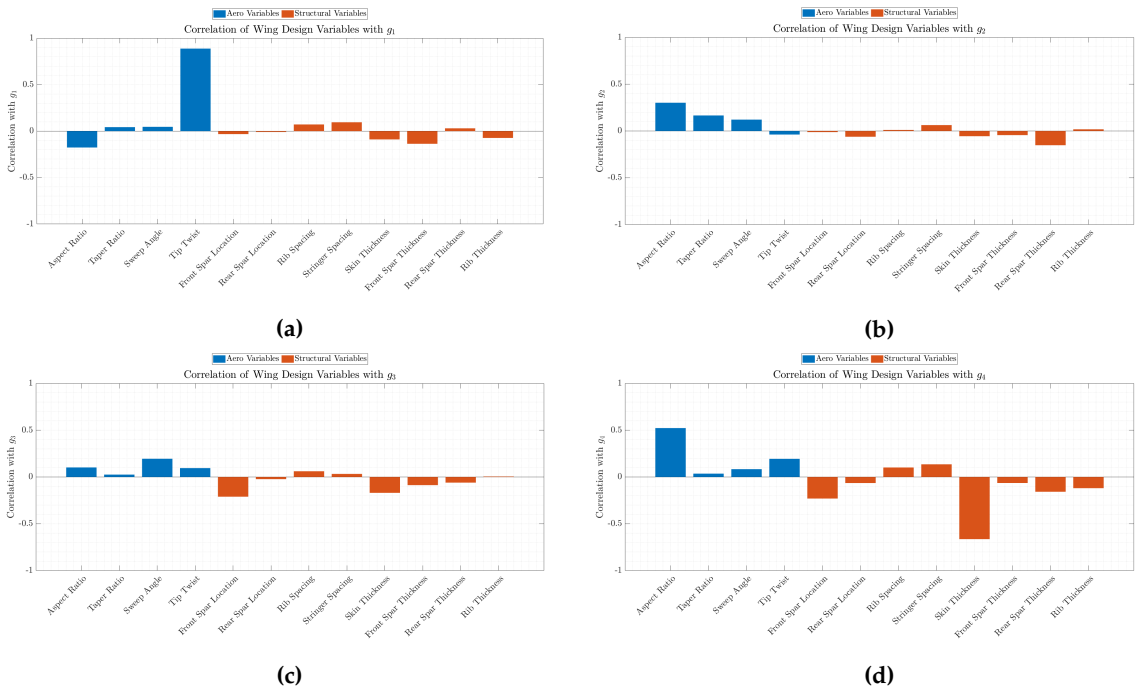

Figure A8. 2^{nd} SBO iter. - Correlation of aerodynamic and structural design parameters with g_1 (**a**), g_2 (**b**), g_3 (**c**), and g_4 (**d**).

Appendix A.3. 3^{rd} *DoE*

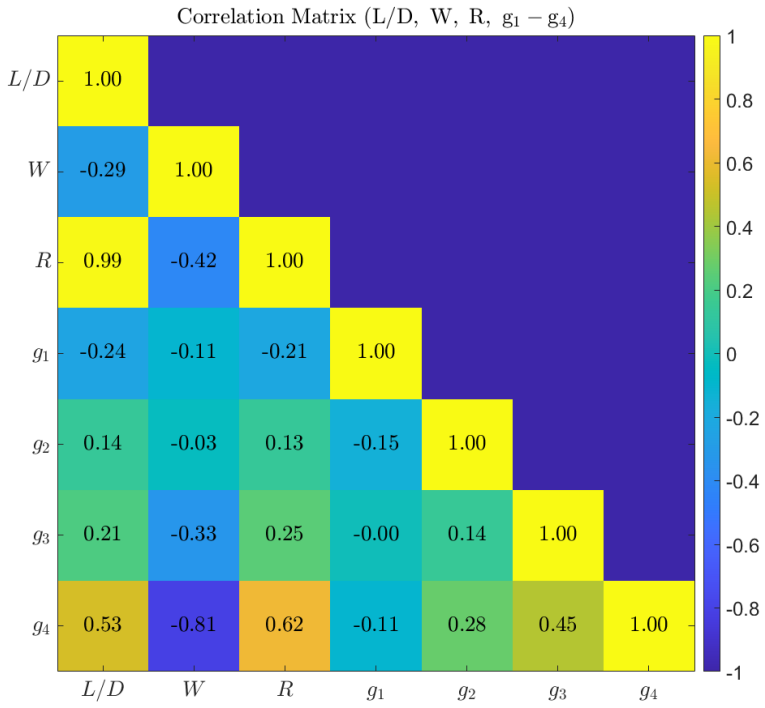

Figure A9. 3^{rd} SBO iter. - Correlation between objective and constraints.

 doi:10.20944/preprints202603.1960.v1

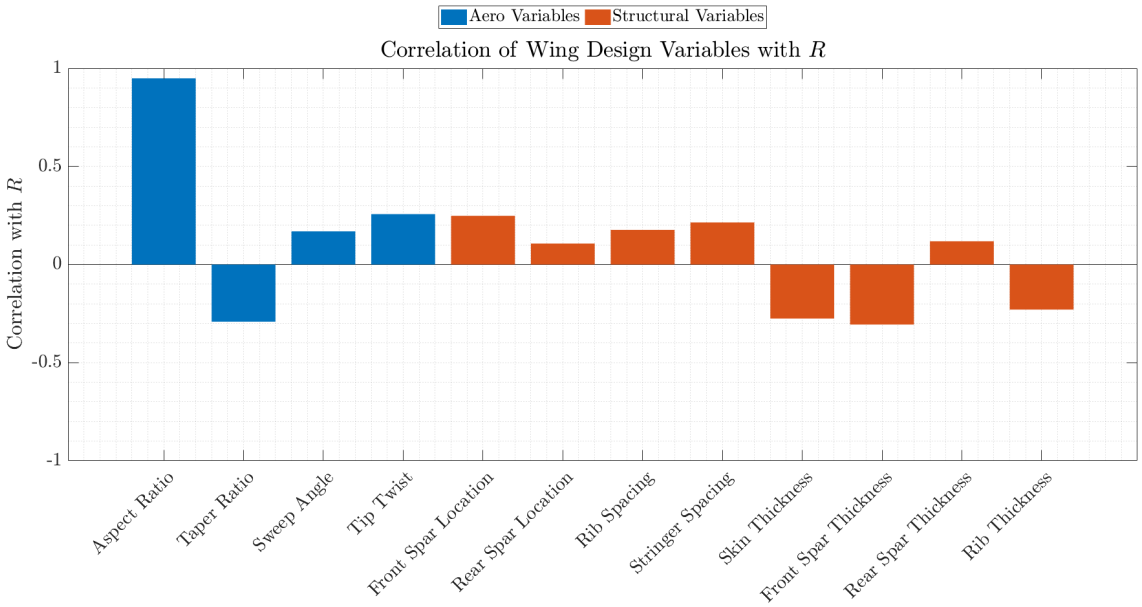

Figure A10. 3^{rd} SBO iter. - Correlation of aerodynamic and structural design parameters with Range-Objective.

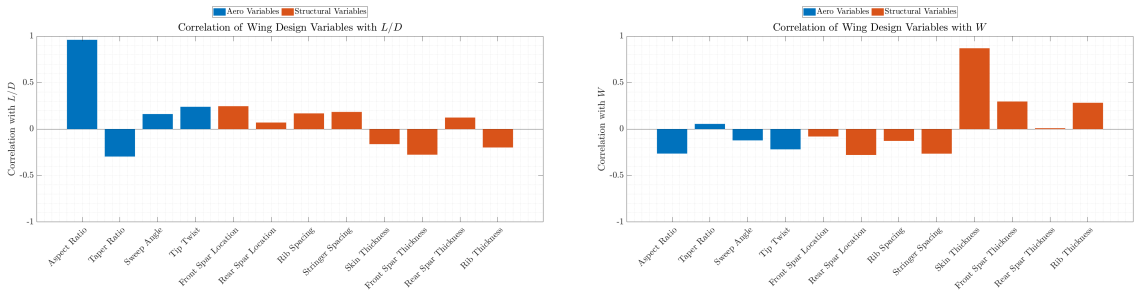

(a) **(b)**

Figure A11. 3^{rd} SBO iter. - Correlation of aerodynamic and structural design parameters with L/D (**a**), and *Weight* (**b**).

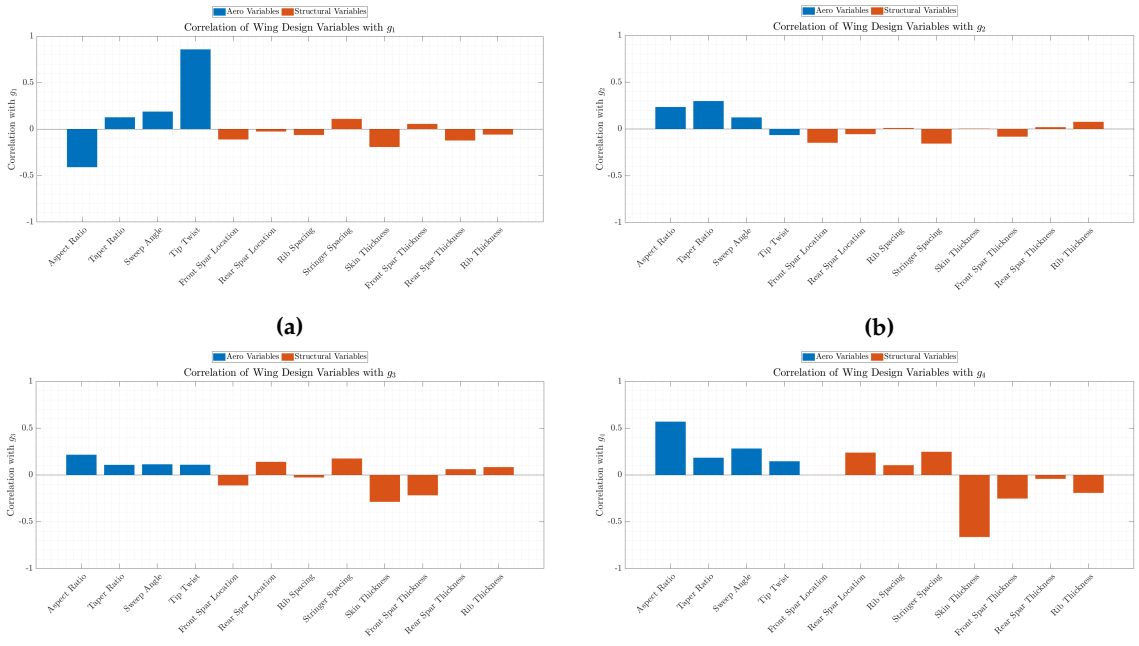

(a) **(b)**

(c) **(d)**

Figure A12. 3^{rd} SBO iter. - Correlation of aerodynamic and structural design parameters with g_1 (**a**), g_2 (**b**), g_3 (**c**), and g_4 (**d**).

 doi:10.20944/preprints202603.1960.v1

Appendix A.4. 4^{th} DoE

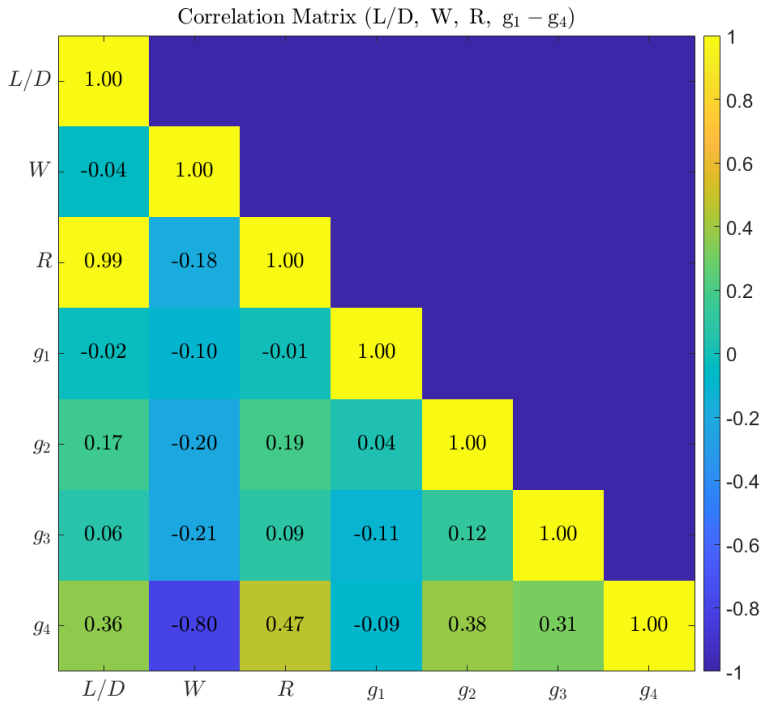

Figure A13. 4^{th} SBO iter. - Correlation between objective and constraints.

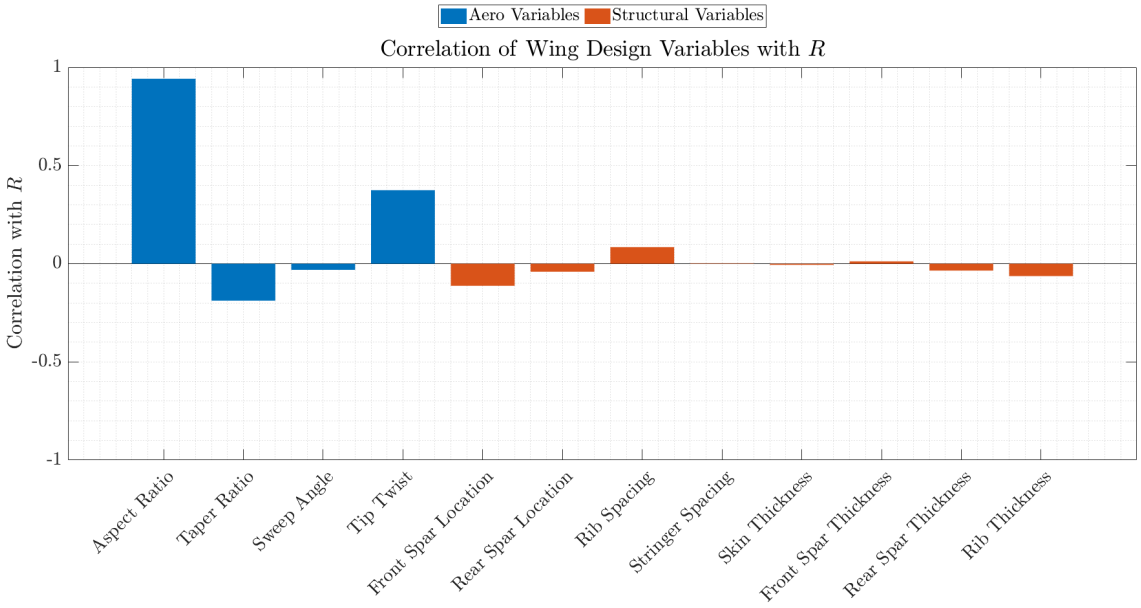

Figure A14. 4^{th} SBO iter. - Correlation of aerodynamic and structural design parameters with Range-Objective.

 doi:10.20944/preprints202603.1960.v1

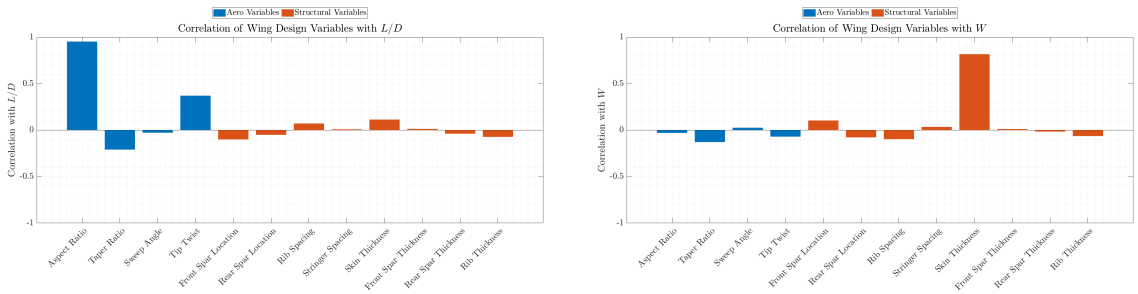

(a) **(b)**

Figure A15. 4^{th} SBO iter. - Correlation of aerodynamic and structural design parameters with L/D (**a**), and *Weight* (**b**).

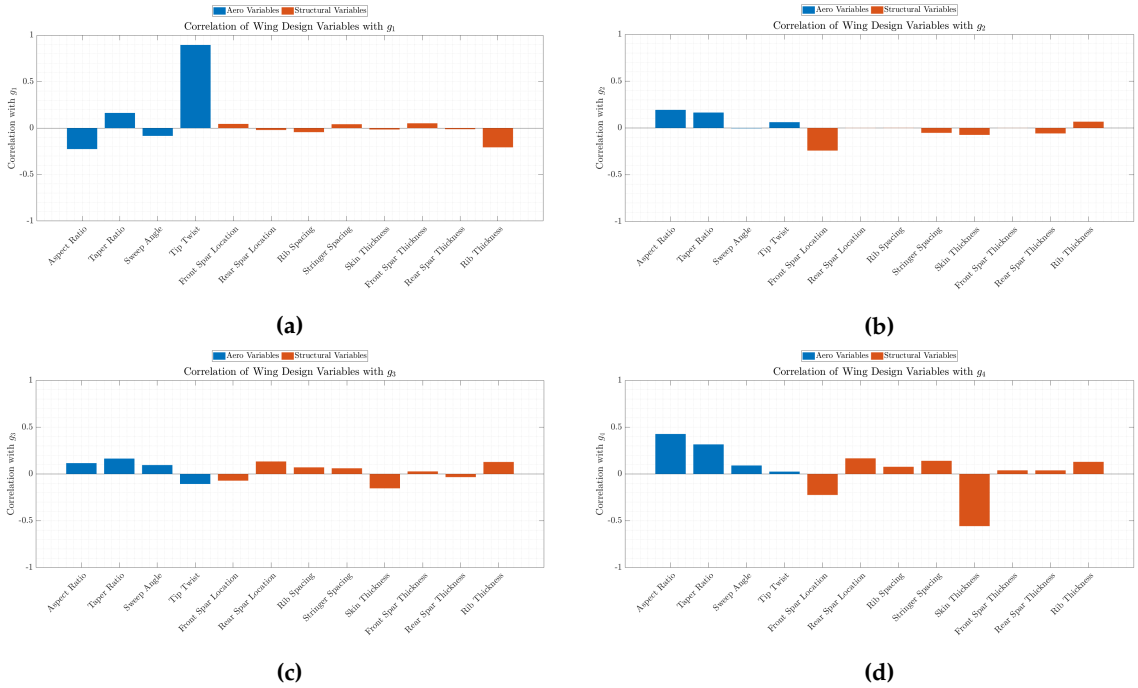

(a) **(b)**

(c) **(d)**

Figure A16. 4^{th} SBO iter. - Correlation of aerodynamic and structural design parameters with g_1 (**a**), g_2 (**b**), g_3 (**c**), and g_4 (**d**).

References

1. Lyu, Z.; Kenway, G.K.W.; Martins, J.R.R.A. Aerodynamic Shape Optimization Investigations of the Common Research Model Wing Benchmark. *AIAA Journal* **2015**, *53*, 968–985, [https://doi.org/10.2514/1.J053318]. https://doi.org/10.2514/1.J053318.
2. Chen, S.; Lyu, Z.; Kenway, G.K.W.; Martins, J.R.R.A. Aerodynamic Shape Optimization of Common Research Model Wing–Body–Tail Configuration. *Journal of Aircraft* **2016**, *53*, 276–293, [https://doi.org/10.2514/1.C033328]. https://doi.org/10.2514/1.C033328.
3. Ghafoorian, F.; Wan, H.; Chegini, S. A Systematic Analysis of a Small-Scale HAWT Configuration and Aerodynamic Performance Optimization Through Kriging, Factorial, and RSM Methods. *Journal of Applied and Computational Mechanics* **2024**, pp. –. https://doi.org/10.22055/jacm.2024.47896.4822.
4. Zheng, B.; Moni, A.; Yao, W.; Xu, M. Manifold Learning for Aerodynamic Shape Design Optimization. *Aerospace* **2025**, *12*. https://doi.org/10.3390/aerospace12030258.
5. Kilimtzidis, S.; Dimitriadis, G.; Kostopoulos, V., A Novel Surrogate-Assisted Structural Optimization Framework for Full-Aircraft Configurations. In *AIAA SCITECH 2026 Forum*; [https://arc.aiaa.org/doi/pdf/10.2514/6.2026-0581]. https://doi.org/10.2514/6.2026-0581.
6. Kilimtzidis, S.; Kotzakolios, A.; Kostopoulos, V. Efficient structural optimisation of composite materials aircraft wings. *Composite Structures* **2023**, *303*, 116268. https://doi.org/10.1016/j.compstruct.2022.116268.
7. Miki, M.; Sugiyama, Y. Optimum design of laminated composite plates using lamination parameters. *AIAA Journal* **1993**, *31*, 921–927.

 doi:10.20944/preprints202603.1960.v1

8. Fukunaga, H.; Sekine, H.; Sato, M. Bending-twisting coupling effects on the fundamental frequency of laminated composite plates. *Composite Structures* **1994**, *28*, 355–362.
9. Liu, B.; Haftka, R.T.; Akgun, M.A. Two-level composite wing structural optimization using lamination parameters. *Structural and Multidisciplinary Optimization* **2004**, *26*, 329–341.
10. Calderon, D.E.; Mader, C.A.; Martins, J.R.R.A. Aeroelastic tailoring of a high-aspect-ratio wing using geometrically nonlinear analysis. *AIAA Journal* **2018**, *56*, 4021–4036.
11. Calderon, D.E.; Mader, C.A.; Martins, J.R.R.A. Impact of geometric nonlinearities on aircraft wing structural optimization. *Structural and Multidisciplinary Optimization* **2019**, *60*, 159–176.
12. Triplett, W.E. A multidisciplinary approach to aeroelastic optimization. PhD thesis, U.S. Air Force Institute of Technology, 1980.
13. Love, M.H.; Bohlman, J.D. Aeroelastic optimization of composite wings. *Journal of Aircraft* **1989**, *26*, 918–924.
14. Haftka, R.T. Optimization of flexible wing structures. *Journal of Aircraft* **1973**, *10*, 725–731.
15. Haftka, R.T. Integrated aerodynamic-structural design. *AIAA Journal* **1977**, *15*, 350–356.
16. Grossman, B.; Strauch, G.J.; Eppard, W.M. Integrated aerodynamic-structural design of a sailplane wing. *Journal of Aircraft* **1988**, *25*, 855–861.
17. Grossman, B.; Haftka, R.T.; Kao, P.J. Integrated aerodynamic-structural optimization using sensitivity derivatives. *Journal of Aircraft* **1990**, *27*, 985–992.
18. Reuther, J.J.; Alonso, J.J.; Jameson, A. Aerodynamic-structural optimization of wing shapes for Euler flow. *AIAA Journal* **1999**, *37*, 312–320.
19. Maute, K.; Allen, M.; Ramm, E. Coupled aeroelastic optimization of flexible wings. *AIAA Journal* **2001**, *39*, 2055–2064.
20. Martins, J.R.R.A.; Alonso, J.J.; Reuther, J.J. High-fidelity aero-structural design optimization of a supersonic business jet. *Journal of Aircraft* **2004**, *41*, 523–530.
21. Barcelos, M.; Maute, K. A Schur-Newton-Krylov solver for steady-state aeroelastic analysis. *AIAA Journal* **2006**, *44*, 629–640.
22. Barcelos, M.; Maute, K. Integrated aeroelastic optimization using RANS-based CFD. *Computers & Structures* **2008**, *86*, 1193–1207.
23. Kenway, G.K.W.; Martins, J.R.R.A. Multipoint high-fidelity aerostructural optimization of aircraft configurations. *Journal of Aircraft* **2014**, *51*, 144–160.
24. Lyu, Z.; Kenway, G.K.W.; Martins, J.R.R.A. Aerodynamic shape optimization of the Common Research Model wing. *AIAA Journal* **2015**, *53*, 968–985.
25. Gray, J.S. High-fidelity aerostructural optimization of aircraft wings. PhD thesis, University of Michigan, 2021.
26. Nikolaou, E.; Kilimtzidis, S.; Kostopoulos, V. Winglet Design for Aerodynamic and Performance Optimization of UAVs via Surrogate Modeling. *Aerospace* **2025**, *12*, 36. https://doi.org/10.3390/aerospace12010036.
27. Benaouali, A.; Kachel, S. Multidisciplinary design optimization of aircraft wing using commercial software integration. *Aerospace Science and Technology* **2019**, *92*, 766–776. https://doi.org/10.1016/j.ast.2019.06.040.
28. Nikolaou, E.; Kilimtzidis, S.; Kostopoulos, V. Multi-Fidelity Surrogate-Assisted Aerodynamic Optimization of Aircraft Wings. *Aerospace* **2025**, *12*. https://doi.org/10.3390/aerospace12040359.
29. Ansys, Inc., Canonsburg, PA. *Ansys Fluent User's Guide*, 2023. Accessed: 2023-03-27.
30. Spalart, P.; Allmaras, S. A one-equation turbulence model for aerodynamic flows. In Proceedings of the 30th Aerospace Sciences Meeting and Exhibit. American Institute of Aeronautics and Astronautics, 1992. https://doi.org/10.2514/6.1992-439.
31. Kassapoglou, C. *Design and Analysis of Composite Structures*; John Wiley & Sons Ltd, 2013. https://doi.org/10.1002/9781118536933.
32. Marlett, K. HEXCEL 8552 IM7 Unidirectional Prepreg 190 gsm 35% RC Qualification Statistical Analysis Report,Rept. NCP-RP-2009-028 Rev B. Technical report, National Institute for Aviation Research, 2011.
33. Alexandrov, N.M.; Dennis, J.E.; Lewis, R.M.; Torczon, V. A trust-region framework for managing the use of approximation models in optimization. *Structural Optimization* **1998**, *15*, 16–23. https://doi.org/10.1007/bf01197433.
34. McKay, M.D.; Beckman, R.J.; Conover, W.J. Comparison of Three Methods for Selecting Values of Input Variables in the Analysis of Output from a Computer Code. *Technometrics* **1979**, *21*, 239–245. https://doi.org/10.1080/00401706.1979.10489755.
35. Jones, D.R. A Taxonomy of Global Optimization Methods Based on Response Surfaces. *Journal of Global Optimization* **2001**, *21*, 345–383. https://doi.org/10.1023/a:1012771025575.

 doi:10.20944/preprints202603.1960.v1

36. Forrester, A.I.J.; Sóbester, A.; Keane, A.J. *Engineering Design via Surrogate Modelling*; Wiley, 2008. https://doi.org/10.1002/9780470770801.
37. Forrester, A.I.; Sóbester, A.; Keane, A.J. Multi-fidelity optimization via surrogate modelling. *Proceedings of the Royal Society A: Mathematical, Physical and Engineering Sciences* **2007**, *463*, 3251–3269. https://doi.org/10.1098/rspa.2007.1900.